

# Single-stage gradient-based stellarator coil design: Optimization for near-axis quasi-symmetry

Andrew Giuliani<sup>a</sup>, Florian Wechsung<sup>a</sup>, Antoine Cerfon<sup>a</sup>, Georg Stadler<sup>a</sup>, Matt Landreman<sup>b</sup>

<sup>a</sup>*Courant Institute of Mathematical Sciences, New York University, New York, New York, USA*

<sup>b</sup>*University of Maryland-College Park, Maryland, USA*

---

## Abstract

We present a new coil design paradigm for magnetic confinement in stellarators. Our approach directly optimizes coil shapes and coil currents to produce a vacuum quasi-symmetric magnetic field with a target rotational transform on the magnetic axis. This approach differs from the traditional two-stage approach in which first a magnetic configuration with desirable physics properties is found, and then coils to approximately realize this magnetic configuration are designed. The proposed single-stage approach allows us to find a compromise between confinement and engineering requirements, i.e., find easy-to-build coils with good confinement properties. Using forward and adjoint sensitivities, we derive derivatives of the physical quantities in the objective, which is constrained by a nonlinear periodic differential equation. In two numerical examples, we compare different gradient-based descent algorithms and find that incorporating approximate second-order derivative information through a quasi-Newton method is crucial for convergence. We also explore the optimization landscape in the neighborhood of a minimizer and find many directions in which the objective is mostly flat, indicating ample freedom to find simple and thus easy-to-build coils.

*Keywords:* stellarator optimization, quasi-symmetry, adjoint/forward sensitivity, optimal control, magnetic confinement

---

## 1. Introduction

Stellarators are a promising candidate for magnetic confinement fusion, in which a high-temperature plasma is confined by a magnetic field that lacks continuous rotation symmetry (axisymmetry) [6, 18]. This field is produced by electromagnetic coils, and these coils are designed using optimization targeting a multitude of desired stellarator properties. Mathematically, this amounts to complicated optimization objectives with components that may be in competition with each other, governed by complex physics equations [22, 34, 39]. At the same time, the optimization must be formulated to avoid coil shapes that are impractical to build [24, 35, 47]. Numerical optimization for these problems is challenging due to the nonlinearity of the governing equations, complicated minimization landscapes, and the difficulty in obtaining accurate derivatives. In this article, we propose a new formulation of this optimization problem in which the coil parameters are the primary optimization unknowns, and which therefore avoids the indirect, two-stage approach currently used by the stellarator community. We use our new formulation to design coils for vacuum stellarator configurations, and illustrate in these optimization problems the advantages of using analytical derivatives of the objective with respect to parameters in the coil representation.

From a physical point of view, the optimization problem may be motivated by highlighting the major weaknesses of stellarators as compared to their currently better performing cousin, the tokamak, which is a toroidally axisymmetric device with generally simpler coils [19]. First, unlike in tokamaks, the orbits of single particles not subject to collisions are not guaranteed to be confined in a generic stellarator. Particle and energy losses can therefore be unacceptably high [18, 19, 41] if the equilibrium magnetic configuration

is not designed with care, which can lead to significant deterioration and damage of the first wall, and requiring unacceptably high power to maintain the plasma temperature. Second, planar coils are usually not sufficient to produce the desired equilibrium magnetic field, and stellarators commonly require highly distorted coils, which are expensive and complex to build [24, 35, 47]. In the last four decades, a family of magnetic fields guaranteeing good confinement, named quasi-symmetric magnetic fields [18], has been identified and studied extensively [5, 9, 37]. It is the design basis for several advanced stellarators that have been partially constructed or proposed for future experiments [1, 13, 14, 20, 25, 31, 53]. While other families of magnetic fields may lead to equally good confinement [18], quasi-symmetric fields are convenient from a mathematical point of view because there are several equivalent formulations for the quasi-symmetry condition, which are all fairly easy to compute numerically. In this article, we will therefore focus on quasi-symmetric magnetic configurations.

Regarding coil design, the following optimization strategy has been favored in the past, which we call the indirect method or the two-stage approach in this article. In the first stage, coils are ignored and we optimize the shape of the toroidal boundary surface of the plasma. The field is assumed tangent to the boundary, enabling the interior field to be computed from the boundary shape. The objective function reflects physics properties of the plasma inside the surface. In the second optimization stage, the magnetic field determined in the first stage is fixed and we optimize the shapes and currents of electromagnetic coils such that they reproduce this target field [8, 12, 33, 45, 46, 54]. There are several advantages to this approach. It is efficient, since codes computing the magnetic configuration taking as input a known plasma boundary surface on which the magnetic field is tangent (so-called “fixed-boundary equilibrium codes”) are faster and more robust than codes which instead solve for the magnetic configuration taking as input the geometry of the coils and their currents, and for which the location of the toroidal plasma boundary is one of the outputs of the computation (so-called “free-boundary equilibrium codes”). One also empirically observes that with the two-stage method, the level sets of the magnetic flux inside the plasma often are toroidal surfaces foliating a large fraction of the plasma volume, which is the most basic – but not sufficient – requirement for confinement. Furthermore, new methods have been recently proposed to more efficiently optimize coils and reduce their complexity in this two-stage method [26, 38, 54]. The two-stage method has been used for the design of many successful stellarator experiments that are optimized for particle confinement and are currently operating. However, this approach has drawbacks. First, when a stellarator is constructed, one builds coils, and not a plasma boundary; the first stage of the two-stage method thus optimizes for aspects of the experiment on which one does not have direct control. Undesired discrepancies in the magnetic field necessarily arising from the coil design process in the second stage may then significantly alter the quality of the equilibrium magnetic configuration. Conversely, the two-stage method cannot capture magnetic configurations that are achievable with relatively simple coils. For example, existing three-dimensional equilibrium codes are not able to compute equilibria for which the plasma boundary has corners, corresponding to separatrices. Third, the two-stage approach makes it difficult to balance desired physics properties with coil manufacturing constraints.

A single-stage approach designs optimized stellarators starting directly from coil configurations. It holds the promise to address these drawbacks, reduce the complexity of stellarator coils, improve access to the device, and therefore help to reduce construction costs. However, to the best of our knowledge, a systematic and robust method for obtaining magnetic fields with good confinement properties has never been proposed for that single-stage method. This is particularly challenging since most coil shapes generate magnetic fields whose level sets of the magnetic flux are not closed toroidal surfaces for a large fraction of the plasma volume, i.e. fields which do not satisfy the most basic requirements for confinement. The purpose of the present article is to demonstrate that a single-stage coil optimization method can be developed that addresses that challenge. Our strategy is to optimize coils so they produce a magnetic field that approximates, on the magnetic axis, the quasi-symmetric field constructed with the Garren-Boozer near-axis expansion [15, 28–30] as well as its gradient, and which also has a near-axis rotational transform that is close to a target rotational transform chosen as an input. We recall that the magnetic axis is the closed curve corresponding to the innermost level set of the magnetic flux [18], see for instance the dotted line in Figure 8. Additionally, recall that the rotational transform,  $\iota$ , is

a property of the magnetic field and its field lines that plays an important role for confinement [18]. The rotational transform at the axis is given by the number of poloidal transits per toroidal transit for field lines in the neighborhood of the axis. Mathematically, we solve an optimization problem that is constrained by a nonlinear differential equation. Building on methods from optimization governed by differential equations [7, 17, 40], we derive analytical expressions for the gradients of the optimization objective. Following a discretize-then-optimize approach, in which we discretize the governing equation and compute the analytical derivatives, using either forward or adjoint sensitivities, at the discrete level, we have the guarantee of obtaining discretely exact gradients, which is advantageous for iterative descent optimization algorithms [17].

### *1.1. Contributions and limitations*

We make the following contributions. (1) We present a single-stage approach to stellarator coil design, which directly targets quasi-symmetry and avoids the two-stage optimization process that is currently favored by the stellarator community. This allows a more thorough exploration of the trade-offs between confinement and engineering constraints, and thus, it has the potential to help design coils that are easier and more cost-effective to manufacture. (2) We derive analytical derivatives of physical quantities (e.g., the rotational transform on an axis) in the objective. This is made possible by choosing suitable characterizations of these quantities, combined with forward and adjoint sensitivity methods for objectives governed by differential equations. Accurate derivatives facilitate efficient numerical solution and enable exploration of the optimization objective landscape, but are not commonly used in stellarator optimization codes. (3) A numerical study of the Hessian at a minimum of the objective provides some insight into to objective landscape. Namely, there is only a moderate number of directions in parameter space where the Hessian has large curvature and thus the objective is very sensitive to changes in these directions. In many other directions, the objective is mostly flat, indicating ample freedom for finding coil configurations with good confinement properties that are simpler and thus easier-to-build.

Our approach also has several limitations. (1) The presented approach currently focuses on vacuum magnetic configurations, i.e., it neglects magnetic fields generated by currents inside the plasma. At the end of this article, we discuss generalizations of the present approach to include these contributions, which can be important for stellarator experiments with high plasma pressure. (2) While our approach targets quasi-symmetry on and in a neighborhood of the magnetic axis, we do not have explicit control of quasi-symmetry away from the axis. In the last section of this article, we discuss how our method can be extended to enforce quasi-symmetry also on surfaces away from the axis. (3) Our physics and engineering constraints are simpler than those which are imposed in detailed stellarator design studies. The purpose of the present work is to demonstrate the feasibility and the advantages of the single-stage method for the design of quasi-symmetric stellarators. Both the objective and constraints discussed in this article can be expanded depending on the design needs, in which case additional analytical derivatives would have to be computed.

### *1.2. Structure of article*

The structure of this article is as follows. In section 2, we review the equations describing quasi-symmetric magnetic fields near the magnetic axis. In section 3, we present our optimization problem, define our optimization space, and motivate our cost function physically. In section 4, we explain how the forward sensitivity method and the adjoint method each allows us to efficiently and accurately evaluate the gradient with respect to the design parameters, which we need in order to minimize our cost function. We present the magnetic configurations obtained with this new single-stage approach in sections 5 and 6, and summarize our results and suggest future directions for this work in section 7.

## **2. Near-axis quasi-symmetry**

Our optimization formulation aims to find a coil system such that the magnetic field at the magnetic axis is quasi-symmetric, a highly desirable property for confinement. While a quasi-symmetric magnetic

field would be desirable throughout the entire plasma region, published results show that this might not be achievable as the required system of equations is over-determined [15]. Thus, we limit ourselves to finding a quasi-symmetric magnetic field in a neighborhood of the magnetic axis. Instead of considering the axis induced by the magnetic coils, we parameterize a so-called expansion axis independently and include these parameters in the optimization. The optimization problem detailed in section 3 then aims to minimize the difference between the magnetic field induced by the coils and a quasi-symmetric magnetic field derived from a near-axis expansion at that independent axis. This expansion was recently presented in [28–30] and is based on the Garren-Boozer expansion [15]. Upon convergence of the optimization problem detailed in section 3, the magnetic field from the coils and the axis expansion coincide in a neighborhood of the independent axis. In particular, the magnetic axis and the expansion axis coincide and the field induced by the coils is quasi-symmetric close to these axes. Before presenting the optimization problem, we summarize elements of this near-axis expansion that are critical to the understanding of our optimization formulation.

The remainder of this section describes how the choice of an expansion axis and of a value  $\bar{\eta} \in \mathbb{R} \setminus \{0\}$  uniquely defines the quasi-symmetric field  $\mathbf{B}_{\text{QS}}$  and its gradient  $\nabla \mathbf{B}_{\text{QS}}$  on axis. This nonlinear relationship requires to first solve a nonlinear system containing an ordinary differential equation (see (1)) for a function  $\sigma(\phi)$  and  $\iota \in \mathbb{R}$ . These quantities then define the near-axis expansion of the quasi-symmetric magnetic field in terms of  $\sigma$  and  $\iota$ . These technical expressions, which were derived in [27], will be given in (2) and (3) below. Note that  $\sigma$  is a function that is used in the formula for the gradient of the quasisymmetric magnetic field (3), and  $\iota$  is the rotational transform on axis.

We consider the expansion to the order used in [30], such that quasi-symmetry is guaranteed through first order in the distance from the axis, but quasi-symmetry-breaking errors generally arise at second order. In what follows, we assume that the current density on axis is zero, and that the magnetic field is stellarator symmetric [11], and has discrete rotational symmetry. Stellarator symmetry and discrete rotational symmetry imply that in cylindrical coordinates the magnetic field  $\mathbf{B} = (B_R, B_\phi, B_Z)$  satisfies respectively

$$\begin{aligned} B_R(R, \phi, Z) &= -B_R(R, -\phi, -Z), & B_R(R, \phi, Z) &= B_R(R, \phi + 2\pi/N_{\text{fp}}, Z), \\ B_\phi(R, \phi, Z) &= B_\phi(R, -\phi, -Z), & \text{and } B_\phi(R, \phi, Z) &= B_\phi(R, \phi + 2\pi/N_{\text{fp}}, Z), \\ B_Z(R, \phi, Z) &= B_Z(R, -\phi, -Z), & B_Z(R, \phi, Z) &= B_Z(R, \phi + 2\pi/N_{\text{fp}}, Z), \end{aligned}$$

where  $N_{\text{fp}}$  is the number of identical field periods; see also an illustration of these symmetries for coils in Figure 1. The quasi-symmetric expansion field then depends on two inputs, namely the geometry of the expansion axis, and a parameter  $\bar{\eta} \in \mathbb{R} \setminus \{0\}$  that influences how elongated the magnetic surfaces are. The expansion axis may be any closed curve with non-vanishing curvature,  $\Gamma_{\mathbf{a}}(\phi)$ , where  $\phi$  is the standard cylindrical angle. The quasi-symmetric field corresponding to a given axis and  $\bar{\eta}$  is found by first solving the following  $2\pi/N_{\text{fp}}$ -periodic first-order ordinary differential equation with quadratic nonlinearity for  $\sigma = \sigma(\phi)$  and  $\iota \in \mathbb{R}$ :

$$\begin{aligned} \frac{|G_0|}{\ell' B_0} \frac{d\sigma}{d\phi} + (\iota - N) \left[ \frac{\bar{\eta}^4}{\kappa^4} + 1 + \sigma^2 \right] + \frac{2G_0 \bar{\eta}^2 s_\psi \tau}{B_0 \kappa^2} &= 0, \\ \sigma(0) &= 0, \end{aligned} \tag{1}$$

where  $N_{\text{fp}}$  is the number of field periods. The expansion axis enters (1) through its curvature  $\kappa$  and torsion  $\tau$ . Note that the condition  $\sigma(0) = 0$  follows from stellarator symmetry and that the  $2\pi/N_{\text{fp}}$ -periodicity implies that  $\sigma(2\pi/N_{\text{fp}}) = 0$ . Additionally,  $\sigma$  must be odd for stellarator symmetry, so  $\sigma(\pi/N_{\text{fp}}) = 0$  as well. Since  $\iota$  is part of the solution, (1) is not a standard differential equation boundary value problem. However, it is shown in [30] that given a suitable expansion axis with non-vanishing curvature and  $\bar{\eta}$ , the solution pair  $\sigma(\phi)$ ,  $\iota$  of (1) is unique. The constants in (1) are  $G_0 = s_G B_0 L / (2\pi)$ ,  $L$  is the axis length,  $s_G = \pm 1$  specifies if the magnetic field points in the same or opposite direction of increasing  $\phi$ ,  $s_\psi = \pm 1$  is related to the sign of  $\iota$ ,  $B_0$  is a constant,  $\ell' := \|\Gamma'_a(\phi)\|$  is the incremental



axis length, and the integer  $N$  indicates the type of quasi-symmetry. In this paper we only consider quasi-axisymmetry, which is characterized by  $N = 0$ .

Solving (1), we obtain the on-axis rotational transform  $\iota$  and a function  $\sigma(\phi)$ . Once they are known, the quasi-symmetric magnetic field  $\mathbf{B}_{\text{QS}}$  and its gradient  $\nabla\mathbf{B}_{\text{QS}}$  are determined by the formulae [27]

$$\mathbf{B}_{\text{QS}} = B_0 \mathbf{t} \quad (2)$$

and

$$\begin{aligned} \nabla B_{\text{QS},j}(\phi) = s_\psi \frac{B_0^2}{|G_0|} \left\{ \left[ s_\psi \frac{G_0}{B_0} \kappa t_j + \left( \widetilde{X}'_{1c} Y_{1s} + \iota X_{1c} Y_{1c} \right) n_j \right. \right. \\ \left. \left. + \left( \widetilde{Y}'_{1c} Y_{1s} - \widetilde{Y}'_{1s} Y_{1c} + s_\psi \frac{G_0}{B_0} \tau + \iota (Y_{1s}^2 + Y_{1c}^2) \right) b_j \right] \mathbf{n} \right. \\ \left. + \left[ \left( -s_\psi \frac{G_0}{B_0} \tau - \iota X_{1c}^2 \right) n_j + \left( X_{1c} \widetilde{Y}'_{1s} - \iota X_{1c} Y_{1c} \right) b_j \right] \mathbf{b} \right\} + \kappa s_G B_0 n_j \mathbf{t}, \end{aligned} \quad (3)$$

where the  $j$  subscripts indicate Cartesian components,  $\mathbf{t}, \mathbf{n}, \mathbf{b}$  are the Frenet vectors [43], i.e., the unit tangential, normal, and binormal vectors associated to the expansion axis  $\Gamma_{\mathbf{a}}(\phi)$ . Moreover,

$$X_{1c}(\phi) = \frac{\bar{\eta}}{\kappa}, \quad Y_{1s}(\phi) = \frac{s_G s_\psi \kappa}{\bar{\eta}}, \quad Y_{1c}(\phi) = \frac{s_G s_\psi \kappa \sigma}{\bar{\eta}},$$

and we use the scaled derivatives

$$\widetilde{X}'_{1c} = \frac{|G_0|}{\ell' B_0} X'_{1c}(\phi), \quad \widetilde{Y}'_{1s} = \frac{|G_0|}{\ell' B_0} Y'_{1s}(\phi), \quad \widetilde{Y}'_{1c} = \frac{|G_0|}{\ell' B_0} Y'_{1c}(\phi). \quad (4)$$

The above expressions for  $B_{\text{QS},j}, \nabla B_{\text{QS},j}$  depend on the expansion axis parameters  $\mathbf{a}$ , which determine the Frenet frame vectors  $\mathbf{t}, \mathbf{n}, \mathbf{b}$ , the incremental axis length  $\ell'$ , curvature  $\kappa$ , and the torsion  $\tau$ . They additionally depend on the solution pair  $\sigma(\cdot), \iota$  computed by solving (1), which requires a suitable expansion axis characterized by  $\mathbf{a}$ . In the next section, we formulate an optimization problem whose objective involves least squares terms for  $B_{\text{QS},j}, \nabla B_{\text{QS},j}$ , which are considered to be functions of  $\mathbf{a}$ .

### 3. Single-stage coil optimization for quasi-symmetry

We aim to find coils and currents that generate a magnetic field that is quasi-symmetric on axis. In our formulation, we treat the coils, their currents, and an expansion axis as parameters, and formulate an objective that ensures that the magnetic field generated by the coils coincides (or is very close to) the quasi-symmetric field on the expansion axis. As a by-product, this typically also means that the expansion axis nearly coincides with the magnetic axis of the field generated by the coils. We emphasize that the quasi-symmetric field is not fixed, i.e., the unknowns associated to the expansion axis and to the coils are allowed to vary.

#### 3.1. Design parameters

The design parameters of our optimization problem are the geometric degrees of freedom associated to the coils and the expansion axis, the coil currents and the scalar  $\bar{\eta}$ . We model stellarator coils as current-carrying filaments in three dimensions. The Cartesian coordinates of the  $i$ th coil,  $\Gamma_c^{(i)}(\theta) = (x^{(i)}(\theta), y^{(i)}(\theta), z^{(i)}(\theta))$ , are given by a Fourier representation, e.g., the  $x$ -coordinate of the curve describing the  $i$ th coil is

$$x^{(i)}(\theta) = c_{x,0}^{(i)} + \sum_{k=1}^{n_p^{\text{coil}}} s_{x,k}^{(i)} \sin(k\theta) + c_{x,k}^{(i)} \cos(k\theta), \quad (5)$$

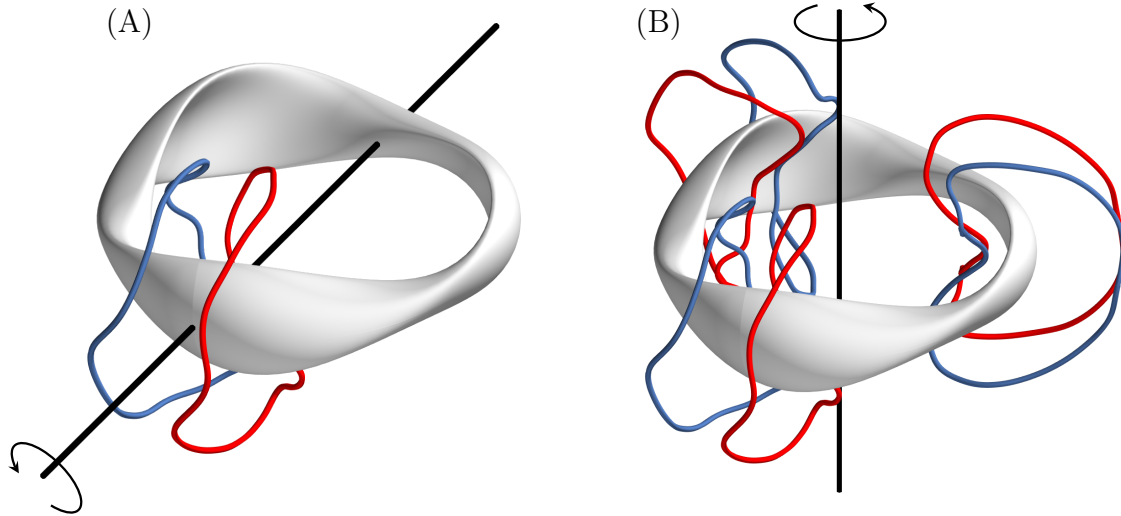


Figure 1: Illustration of stellarator and rotational symmetry. Figure (a) shows a magnetic surface (grey) and a modular coil in the initial NCSX configuration (red) with its stellarator-symmetric counterpart (blue) obtained by a  $180^\circ$  rotation about the  $x$ -axis (black). Figure (b) illustrates discrete rotational symmetry ( $N_{\text{fp}} = 3$ ) by rotating the stellarator symmetric coils from (a) by  $120^\circ$  and  $240^\circ$  around the  $z$ -axis (black).

where  $\theta$  varies from 0 to  $2\pi$ , the real numbers  $c_0^{(i)}$  and  $s_k^{(i)}, c_k^{(i)}$  for  $k = 1 \dots n_p^{\text{coil}}$  are the Fourier coefficients, and  $n_p^{\text{coil}}$  is the number of Fourier modes. The  $y$  and  $z$ -components of the coil curves are defined analogously. In using this (finite) Fourier representation, we are imposing some regularity to the coils. Note that our approach can be adapted to other, local representations that imply less regularity, e.g., splines. The  $i$ th modular coil also has an associated current,  $I_i$ . In total, there are therefore  $6n_p^{\text{coil}} + 3$  unknowns per coil corresponding to the Fourier representation and an additional unknown per coil for the current. The unknowns associated to the coils are combined into the vector of optimization variables  $\mathbf{c} = (c_{x,0}^{(i)}, c_{x,1}^{(i)}, s_{x,1}^{(i)}, \dots, I_0, I_1, \dots)^T \in \mathbb{R}^{N_c(6n_p^{\text{coil}}+4)}$ , which has  $N_c(6n_p^{\text{coil}} + 4)$  entries, where  $N_c$  is the number of modular coils. Note that given a particular coil geometry, the corresponding Fourier representation is not unique. For example, adding a constant angle to  $\theta$  does not affect the coil geometry but produces a different parametrization. However, note that all the terms in the objective defined below only depend on the geometry of the coils and expansion axis and not on their parametrizations. The non-uniqueness of the coil representation may lead to a non-unique representation of minimizers, but the objective value is not affected by this. Additionally, this non-uniqueness is reduced by the fact that the expansion (5) is truncated.

Similar to the coils, we represent the expansion axis,  $\Gamma_{\mathbf{a}}(\phi) = (R(\phi), \phi, Z(\phi))$ , using a Fourier representation for the  $R(\phi)$ ,  $Z(\phi)$  coordinates of the curve in a cylindrical coordinate system. Due to stellarator symmetry,  $R(\phi)$  is only composed of cosines and  $Z(\phi)$  only of sines

$$R(\phi) = R_0 + \sum_{k=1}^{n_p^{\text{axis}}} R_k \cos(kN_{\text{fp}}\phi), \quad Z(\phi) = \sum_{k=1}^{n_p^{\text{axis}}} Z_k \sin(kN_{\text{fp}}\phi),$$

where  $N_{\text{fp}}$  is the number of identical field periods. There is an additional degree of freedom associated to the axis,  $\bar{\eta}$ , that enters in the near-axis expansions. In total, there are  $2n_p^{\text{axis}} + 2$  unknowns associated to the Fourier representation of the axis curve and the additional unknown  $\bar{\eta}$ , both combined into the vector of design parameters  $\mathbf{a} = (R_0, R_1, \dots, Z_1, \dots, \bar{\eta})^T \in \mathbb{R}^{2n_p^{\text{axis}}+2}$ .

### 3.2. Optimization objective

The function that we seek to minimize is

$$\begin{aligned} \hat{J}(\mathbf{c}, \mathbf{a}, \sigma, \iota) &= \frac{1}{2} \int_{\Gamma_{\mathbf{a}}} \|\mathbf{B}_{\text{coils}}(\mathbf{c}) - \mathbf{B}_{\text{QS}}(\mathbf{a})\|^2 dl + \frac{1}{2} \int_{\Gamma_{\mathbf{a}}} \|\nabla \mathbf{B}_{\text{coils}}(\mathbf{c}) - \nabla \mathbf{B}_{\text{QS}}(\mathbf{a}, \sigma, \iota)\|^2 dl \\ &+ \frac{1}{2} \left( \frac{\iota - \iota_{0,a}}{\iota_{0,a}} \right)^2 + R(\mathbf{c}, \mathbf{a}), \end{aligned} \quad (6)$$

where  $\Gamma_{\mathbf{a}}$  is the expansion axis,  $\mathbf{B}_{\text{coils}}$  and  $\nabla \mathbf{B}_{\text{coils}}$  are the magnetic field and its gradient generated by the coils computed using the Biot-Savart law [23],  $\mathbf{B}_{\text{QS}}$  and  $\nabla \mathbf{B}_{\text{QS}}$  are the quasi-symmetric magnetic field and its gradient computed from near-axis expansions (section 2), and  $R(\mathbf{c}, \mathbf{a})$  groups together regularization terms which we describe shortly. The objective is a function of coil and expansion axis variables  $\mathbf{c}$  and  $\mathbf{a}$ , respectively, (section 3.1) and state variables  $\sigma, \iota$  (section 2).

Now, let us discuss the terms in (6) in more detail. The first term forces the on-axis field generated by the coils  $\mathbf{B}_{\text{coils}}$  to coincide with the quasi-symmetric field  $\mathbf{B}_{\text{QS}}$ , where  $\|\cdot\|$  is the standard Euclidean norm. Recall that the quasi-symmetric field on axis and its gradient are computed from the formulae (2) and (3) by solving (1) for  $\sigma$  and  $\iota$ . The second term in (6) acts similarly, but for the gradient of the magnetic field on axis. Since at every point on the axis, the field gradients  $\nabla \mathbf{B}_{\text{coils}}$  and  $\nabla \mathbf{B}_{\text{QS}}$  are  $3 \times 3$  matrices, in this term,  $\|\cdot\|$  denotes the Frobenius norm. The third term forces the on-axis rotational transform  $\iota$  to be close to a given target value  $\iota_{0,a}$ . Similar to  $\mathbf{B}_{\text{QS}}$ ,  $\iota$  is computed by solving (1), i.e., it is a function of the expansion axis geometry and  $\bar{\eta} \in \mathbb{R}$ . Note that in the formulation of the optimization problem, the expansion axis defined by  $\mathbf{a}$  is treated as an independent variable, i.e., during the optimization it is not constrained to being the magnetic axis corresponding to the field from the coils. In fact, we do not require computation of the magnetic axis. However, the first and second penalty terms in (6) tend to become large if the magnetic and the expansion axis differ substantially. Thus, upon convergence, the expansion axis and the magnetic axis (when computed) typically coincide. Treating the expansion axis as independent variable and minimizing the difference between  $\mathbf{B}_{\text{coils}}$  and  $\mathbf{B}_{\text{QS}}$  has proven numerically advantageous compared to considering all computed quantities as functions of the coils.

We now describe multiple regularization terms that we combined in  $R(\mathbf{c}, \mathbf{a})$ . These terms help to find coils (and a magnetic axis) that have desirable engineering properties, e.g., avoid points with large curvature, have a certain length, or are sufficiently far from other coils. We use a number of regularization terms such as

$$\sum_{i=1}^{N_c} \frac{1}{2} \left( \frac{L_c^{(i)}(\mathbf{c}) - L_{0,c}^{(i)}}{L_{0,c}} \right)^2 \quad \text{and} \quad \frac{1}{2} \left( \frac{L_a(\mathbf{a}) - L_{0,a}}{L_{0,a}} \right)^2,$$

which target coil lengths  $L_c^{(i)} > 0$  and an expansion axis length  $L_{0,a} > 0$ . These terms prevent unnecessarily complex coils and impose a target length (and thus a length scale) on the axis. Note that to normalize these regularization terms, they are multiplied by the reciprocal target values. This is also done for the term involving the rotational transform in the objective (6).

One typically wants to avoid coils that contain points with high curvature, as such coils are difficult and thus costly to manufacture. One way to prevent this is to define

$$k_i(\mathbf{c}) = \int_{\Gamma_c^{(i)}} \max(0, \kappa_i - \kappa_{i,0})^4 dl,$$

where  $\Gamma_c^{(i)}$  is the  $i$ th coil,  $\kappa_i$  is the point-wise curvature of coil  $i$ , and  $\kappa_{i,0} := 2\pi/L_c^{(i)}$  is the curvature of a circle with the same target length as coil  $i$ . We use a quartic instead of a quadratic penalty as this more strongly penalizes extremal values. The term  $k_i$  is then used to penalize (an approximation of) the maximum curvature by adding

$$\frac{\delta}{4} \sum_{i=1}^{N_c} k_i(\mathbf{c})$$

to the objective, where  $\delta > 0$  is a regularization weight.

Additionally, we might also want to avoid configurations with coils that are too close to each other. To this end, we denote a minimal distance that we aim for the coils to satisfy by  $d_{\min} > 0$  and for  $i \neq j$  define

$$d_{i,j}(\mathbf{c}) = \int_{\Gamma_{\mathbf{c}}^{(i)}} \int_{\Gamma_{\mathbf{c}}^{(j)}} \max(0, d_{\min} - \|\mathbf{r}_i - \mathbf{r}_j\|)^2 dl_j dl_i,$$

where  $\mathbf{r}_i, \mathbf{r}_j$  is a position on coils  $\Gamma_{\mathbf{c}}^{(i)}, \Gamma_{\mathbf{c}}^{(j)}$ , respectively. Clearly  $d_{i,j}(\mathbf{c}) \geq 0$ , and  $d_{i,j}(\mathbf{c}) > 0$  if and only if the distance between two coils is smaller than  $d_{\min}$  somewhere. This function is once differentiable, and we use  $d_{i,j}(\mathbf{c})$  as quadratic penalty for the minimum distance by adding

$$\frac{\gamma}{2} \sum_{j < i} d_{i,j}(\mathbf{c}) \quad (7)$$

to the objective, where  $\gamma > 0$  is a regularization weight. It is possible to reduce the computational cost of the double sum in (7) by taking into account symmetries and making assumptions on coils that are far away from one another. For the results presented here, we use the double sum for convenience. The minimum distance and maximum curvature regularization terms include the arclength as this has been shown to be important to prevent them from acting in a parametrization-dependent manner [2].

In summary, we want to find a minimizer of  $\hat{J}(\mathbf{c}, \mathbf{a}, \sigma, \iota)$  in equation (6), constrained by the nonlinear first-order ordinary differential equation (1). In practice, we eliminate the dependence of  $\hat{J}$  on  $\sigma, \iota$  using the constraint and optimize over the smaller space  $\mathbf{c}, \mathbf{a}$ .

### 3.3. Discretization

Next, we briefly summarize our discretization of the state equation (1) and the objective (6). To distinguish functions from their finite-dimensional approximations, we use bold letters to denote finite-dimensional approximation vectors, e.g., the function  $\sigma(\phi)$  corresponds to a vector  $\boldsymbol{\sigma} \in \mathbb{R}^{n_\phi}$ .

We approximate the solution to (1),  $\sigma$  and  $\iota$ , using a Fourier pseudo-spectral collocation discretization [30, 51]. The numerical solution,  $(\boldsymbol{\sigma}, \iota) \in \mathbb{R}^{n_\phi+1}$ , then solves the finite-dimensional nonlinear system  $\mathbf{g}(\mathbf{a}, \boldsymbol{\sigma}, \iota) = \mathbf{0} \in \mathbb{R}^{n_\phi+1}$ , the components of which are

$$g_q := \frac{|G_0|}{\ell'_q B_0} D_q \boldsymbol{\sigma} + \iota \left[ \frac{\bar{\eta}^4}{\kappa_q^4} + 1 + \sigma_q^2 \right] + \frac{2G_0 \bar{\eta}^2 s_\psi \tau_q}{B_0 \kappa_q^2} = 0 \text{ for } q = 0 \dots n_\phi - 1, \quad (8)$$

$$g_{n_\phi} := \sigma_0 = 0.$$

Here,  $D_q$  is the  $q$ th row of the spectral differentiation matrix  $D$  on the interval  $[0, 2\pi/N_{\text{fp}})$  with  $n_\phi$  discretization points [51] and  $\sigma_{n_\phi} = 0$  due to periodicity. The approximate solution is  $\boldsymbol{\sigma} = (\sigma_0, \dots, \sigma_{n_\phi-1})^T$ , where  $\sigma_q \approx \sigma(\phi_q)$ ,  $\phi_q = q(2\pi/N_{\text{fp}})/n_\phi$ . Additionally,  $\ell'_q, \tau_q$ , and  $\kappa_q$  are the incremental arc length, torsion and curvature on the expansion axis at  $\phi_q$ .

Integrals are approximated by the trapezoidal rule, using uniformly spaced quadrature points, which is well known to converge spectrally for smooth, periodic functions [48]. Thus, after applying quadrature, the discretized objective function is

$$\begin{aligned} \hat{J}(\mathbf{c}, \mathbf{a}, \boldsymbol{\sigma}, \iota) &= \left( \frac{2\pi}{n_\phi} \right) \sum_{q=0}^{n_\phi-1} \left[ \frac{1}{2} \|\mathbf{B}_{\text{coils},q}(\mathbf{c}) - \mathbf{B}_{\text{QS},q}(\mathbf{a})\|^2 \|\Gamma'_a(\phi_q)\| \right] \\ &+ \left( \frac{2\pi}{n_\phi} \right) \sum_{q=0}^{n_\phi-1} \left[ \frac{1}{2} \|\nabla \mathbf{B}_{\text{coils},q}(\mathbf{c}) - \nabla \mathbf{B}_{\text{QS},q}(\mathbf{a}, \boldsymbol{\sigma}, \iota)\|^2 \|\Gamma'_a(\phi_q)\| \right] + \frac{1}{2} \left( \frac{\iota - \iota_{0,a}}{\iota_{0,a}} \right)^2 + R(\mathbf{c}, \mathbf{a}), \end{aligned} \quad (9)$$

where  $n_\phi$  is the number of equispaced quadrature points on  $[0, 2\pi/N_{\text{fp}})$  of the expansion axis and the subscript  $q$  indicates that the term is evaluated at the  $q$ th quadrature point along the expansion axis. The lengths of the coils and axis in the regularization terms are

$$L_c^{(i)} = \frac{2\pi}{n_\theta} \sum_{r=0}^{n_\theta-1} \|\Gamma_{\mathbf{c}}^{(i)'}(\theta_r)\| \quad \text{and} \quad L_a = \frac{2\pi}{n_\phi} \sum_{q=0}^{n_\phi-1} \|\Gamma_{\mathbf{a}}'(\phi_q)\|, \quad (10)$$

where  $n_\theta$  is the number of quadrature points on each coil, and  $\theta_r = 2r\pi/n_\theta$  is the  $r$ th quadrature point on a coil. Note a slight abuse of notation by using the same symbol  $\hat{J}$  for the continuous objective (6) and its discretization (9).

The quasisymmetric field and its gradient,  $\mathbf{B}_{\text{QS}}, \nabla\mathbf{B}_{\text{QS}}$  in the discrete problem, are straightforward to compute by evaluating (2) and (3) at each quadrature point  $\Gamma_{\mathbf{a}}(\phi_q)$  on the axis. We use the spectral differentiation matrix to determine an approximation of  $\sigma'(\phi_q)$  in (8) as required in (4). The field generated by the coils  $\mathbf{B}_{\text{coils}}$  in the discrete problem are evaluated at each quadrature point on the axis by using the Biot-Savart law, approximated using the trapezoidal rule

$$\mathbf{B}_{\text{coils},q} = \frac{\mu_0}{4\pi} \left( \frac{2\pi}{n_\theta} \right) \sum_{i=1}^{N_c} \sum_{r=0}^{n_\theta-1} I_i \frac{\Gamma_{\mathbf{c}}^{(i)'}(\theta_r) \times [\Gamma_{\mathbf{a}}(\phi_q) - \Gamma_{\mathbf{c}}^{(i)}(\theta_r)]}{\|\Gamma_{\mathbf{a}}(\phi_q) - \Gamma_{\mathbf{c}}^{(i)}(\theta_r)\|^3},$$

The gradient of the magnetic field generated by the coils,  $\nabla\mathbf{B}_{\text{coils},q}$ , is computed in a similar manner. Thus, given the design parameters  $\mathbf{c}$  and  $\mathbf{a}$ , the objective can be evaluated.

#### 4. Analytical computation of derivatives

Next, we summarize available techniques for computing derivatives of optimization problems constrained by complex physics equations. The derivations in this sections are formal, i.e., we assume that all functions are sufficiently smooth and that the Jacobian of the constraint has full rank to guarantee existence of Lagrange multipliers. While these techniques are well-known, we use this section to discuss advantages and disadvantages of different approaches for the stellarator optimization problem. The discrete optimization problem discussed in section 3.3 can be written as

$$\begin{aligned} & \min_{\mathbf{c}, \mathbf{a}, \boldsymbol{\sigma}, \iota} \hat{J}(\mathbf{c}, \mathbf{a}, \boldsymbol{\sigma}, \iota), \\ & \text{subject to } \mathbf{g}(\mathbf{a}, \boldsymbol{\sigma}, \iota) = 0. \end{aligned} \quad (11)$$

Solving (11) requires optimizing  $\hat{J}$  over  $\mathbf{c}$ ,  $\mathbf{a}$ ,  $\boldsymbol{\sigma}$  and  $\iota$  while taking into account the nonlinear equality constraint equation  $\mathbf{g}(\mathbf{a}, \boldsymbol{\sigma}, \iota) = 0$ . When this equality constraint admits a unique solution,  $(\boldsymbol{\sigma}, \iota)$  for a given axis parameters  $\mathbf{a}$ , we can use the implicit function theorem to transform (11) into an equivalent unconstrained problem over a smaller parameter space

$$\min_{\mathbf{c}, \mathbf{a}} J(\mathbf{c}, \mathbf{a}), \quad (12)$$

where  $J(\mathbf{c}, \mathbf{a}) = \hat{J}(\mathbf{c}, \mathbf{a}, \boldsymbol{\sigma}(\mathbf{a}), \iota(\mathbf{a}))$ , and  $\boldsymbol{\sigma}(\mathbf{a}), \iota(\mathbf{a})$  are considered as implicitly defined functions of  $\mathbf{a}$  through the solution of  $\mathbf{g}(\mathbf{a}, \boldsymbol{\sigma}, \iota) = 0$ . The main advantage of (12) compared to (11) is that we have eliminated the equality constraint, allowing us to use methods from unconstrained optimization. However, the implicit dependence of  $(\boldsymbol{\sigma}, \iota)$  on  $\mathbf{a}$  makes the computation of derivatives of  $J$  in (12) challenging. In the following, we summarize the *forward* and *adjoint sensitivity* approaches to compute gradients of  $J$  and illustrate their application to the stellarator optimization problem (12). Our derivations are for the discretized equation and objective, which avoids inconsistencies compared to when derivatives are computed in infinite dimensions, followed by discretization of the resulting equations. Standard references for computation of derivatives for problems constrained by infinite-dimensional ordinary or partial differential equations are [7, 17, 40].

In both, forward and adjoint sensitivity methods, for the optimization problem (12) we have

$$\frac{\partial J}{\partial \mathbf{c}} = \frac{\partial \hat{J}}{\partial \mathbf{c}}. \quad (13)$$

since the coil design parameters ( $\mathbf{c}$ ) do not affect the state variables ( $\boldsymbol{\sigma}, \iota$ ). In contrast, the axis design parameters ( $\mathbf{a}$ ) directly affect the state variables, thus we use either a forward or an adjoint sensitivity approach to determine the gradient of  $J$  with respect to  $\mathbf{a}$ .

#### 4.1. Gradient from forward sensitivities

One approach to computing the gradient of the objective is to use forward sensitivities. Direct application of the chain rule to (12) gives

$$\frac{\partial J}{\partial \mathbf{a}} = \frac{\partial \hat{J}}{\partial \mathbf{a}} + \frac{\partial \hat{J}}{\partial(\boldsymbol{\sigma}, \iota)} \frac{d(\boldsymbol{\sigma}, \iota)}{d\mathbf{a}}, \quad (14)$$

where  $\partial(\boldsymbol{\sigma}, \iota)$  denotes partial differentiation with respect to the components of  $\boldsymbol{\sigma}$  and with respect to  $\iota$ . Next, we differentiate the equality constraint (8) to obtain

$$\frac{\partial \mathbf{g}}{\partial(\boldsymbol{\sigma}, \iota)} \frac{d(\boldsymbol{\sigma}, \iota)}{d\mathbf{a}} = -\frac{\partial \mathbf{g}}{\partial \mathbf{a}}. \quad (15)$$

This identity can be used to compute the sensitivity matrix  $d(\boldsymbol{\sigma}, \iota)/d\mathbf{a}$ , where the computation of each column requires a linear solve with the matrix  $\partial \mathbf{g}/\partial(\boldsymbol{\sigma}, \iota)$  and a different right hand side, namely the columns of  $\partial \mathbf{g}/\partial \mathbf{a}$ . The sensitivity matrix is then used in (14) to compute the gradient  $\partial J/\partial \mathbf{a}$ .

#### 4.2. Gradient using adjoint sensitivities

An alternative approach to computing the analytical gradient of  $J$  is using the adjoint method. The approach can be derived in different ways. Here, we derive it from (14) and (15) by introducing a Lagrange multiplier vector  $\boldsymbol{\lambda}$  as solution of the (linear) adjoint system

$$\begin{bmatrix} \frac{\partial \mathbf{g}}{\partial(\boldsymbol{\sigma}, \iota)} \end{bmatrix}^T \boldsymbol{\lambda} = -\frac{\partial \hat{J}}{\partial(\boldsymbol{\sigma}, \iota)}. \quad (16)$$

Using the definition of  $\boldsymbol{\lambda}$  in (14) shows that the gradient of  $J$  can also be computed as

$$\frac{\partial J}{\partial \mathbf{a}} = \frac{\partial \hat{J}}{\partial \mathbf{a}} + \boldsymbol{\lambda}^T \frac{\partial \mathbf{g}}{\partial \mathbf{a}}. \quad (17)$$

Using the adjoint approach only requires solving the nonlinear state equation (8) for  $\boldsymbol{\sigma}, \iota$  and one linear equation (16) for  $\boldsymbol{\lambda}$ . In particular, the number of equation solves is independent of the number of axis design variables.

The expressions for the partial derivatives used in (13), (16) and (17) are complex and details are provided in Appendix A and Appendix B. However, as an illustration of the adjoint approach, we differentiate here the simple objective function

$$\hat{J}(\mathbf{a}, \iota) = \frac{1}{2} \left( \frac{\iota - \iota_{0,a}}{\iota_{0,a}} \right)^2, \quad (18)$$

with respect to  $\bar{\eta} \in \mathbf{a}$ . Substituting the expressions for  $\hat{J}$  and  $\mathbf{g}$  in (17) and simplifying, the derivative becomes

$$\frac{\partial J}{\partial \bar{\eta}} = \frac{\partial \hat{J}}{\partial \bar{\eta}} + \boldsymbol{\lambda}^T \frac{\partial \mathbf{g}}{\partial \bar{\eta}} = \sum_{i=0}^{n_\phi-1} \lambda_i \left( \frac{4\iota \bar{\eta}^3}{\kappa_i^4} + \frac{4G_0 \bar{\eta} s_\psi \tau_i}{B_0 \kappa_i^2} \right),$$

where  $\boldsymbol{\lambda} = (\lambda_0, \lambda_1, \dots, \lambda_{n_\phi})^T$  solves the adjoint equation (16).

### 4.3. Comparison between forward and adjoint approaches

Next we compare the above approaches to compute gradients in terms of computational efficiency. The forward sensitivity approach requires as many solves of a linearized state equation as there are parameters, where each problem uses the same system matrix but a different right hand side. When the number of parameters is moderate (as for the problem considered in this paper), this linearized system matrix can be assembled and stored. One can thus compute a matrix factorization and reuse it for each linear solve. In contrast, the adjoint method requires only a single linear solve independently of the number of parameters. The adjoint system matrix is the transpose of the linearized state matrix. Thus, if that matrix can be assembled (as in the case here), the adjoint system can be found straightforwardly. When matrices are too large to be assembled and stored, formulation and solution of the adjoint system can be a more substantive challenge, e.g., [7, 17]. For the problems we consider in this article, both methods perform similarly well due to the moderate parameter dimension (usually, a few hundred). Additionally, a dominant cost is the construction of the matrix  $\partial \mathbf{g} / \partial (\boldsymbol{\sigma}, \iota)$  and the vector  $\partial \hat{J} / \partial (\boldsymbol{\sigma}, \iota)$ , which are required for both the forward and adjoint sensitivity methods.

Note that optimization with gradients computed using the adjoint and forward sensitivity approaches vastly outperforms derivative-free optimization methods or gradient-based optimization with finite difference gradients. The performance of derivative-free methods [10] typically degrades with increasing parameter dimension and thus requires many objective evaluations. For the problem considered here, each objective evaluation requires the solution of the nonlinear state equation and is thus expensive. Similarly, computation of gradients with finite differences requires as many objective evaluations, and thus solutions of the nonlinear state equation, as there are design parameters. One cannot reuse matrix factorizations as in the forward sensitivity approach, and the method therefore becomes vastly more expensive. However, finite difference (directional) gradients are a useful tool to verify gradients computed with the forward or adjoint sensitivity approach, as used in the next section.

### 4.4. Implementation and gradient verification

We have implemented the optimization objective and its gradient using the forward and adjoint sensitivity approaches in Python and MATLAB. In both implementations, the evaluation of the magnetic field and its derivatives with the Biot-Savart law is a dominating part of the objective function and gradient evaluation run time. Therefore, we call an optimized C++ implementation of the Biot-Savart law.

Before presenting two stellarator coil optimization problems in Sections 5 and 6, we numerically verify our derivations and implementation of the analytical gradients by comparing with finite-difference gradients. Namely, we compare the directional derivative in a random direction with standard first, second, fourth and sixth-order finite difference approximations. These derivatives are computed at the initial configuration of Example 6. Our results are shown in the left plot of Figure 2. These results are based on forward sensitivities, but we have verified that the adjoint approach gives identical results. As can be seen, the finite difference step size  $h$  is reduced, the difference between the finite difference approximation and the analytical directional gradient is reduced at the expected rate, i.e., at a linear rate for first-order finite differences, a quadratic rate for second-order finite differences, and so on. As expected, we also see that all finite difference approximations are numerically unstable and floating point error eventually leads to an increase of the error again. These results indicate the correctness of our analytical expressions and their implementation for the gradient of the discretized problem (9).

We also observe that standard first-order finite differencing at most gives seven digits of accuracy when the ideal step size  $h$  is chosen. The fourth and sixth order approximations level off at an error of approximately  $10^{-12}$  and  $10^{-14}$  respectively. However, we emphasize that first-order finite differences only require a single additional objective evaluation, whereas the fourth order finite difference approximation requires four evaluations for each directional derivative.

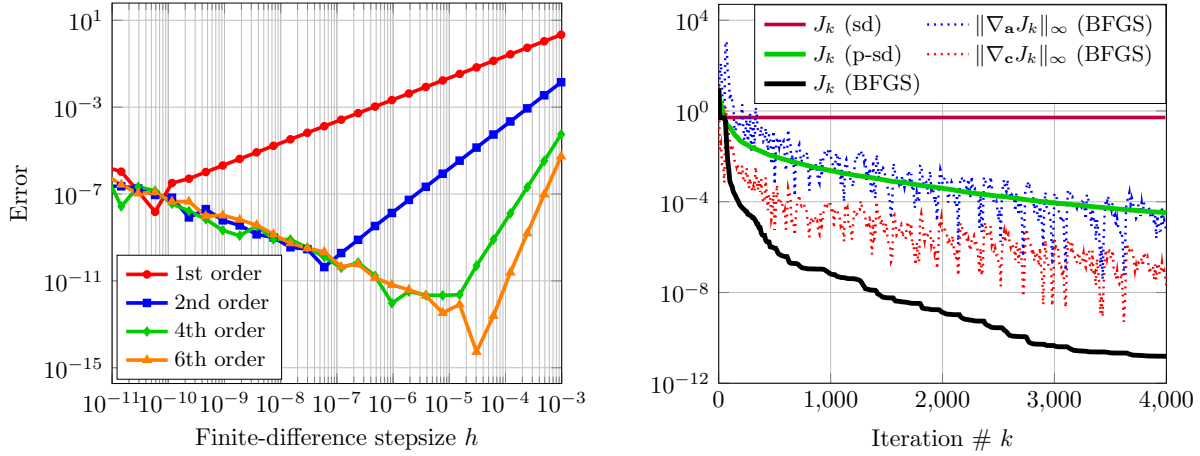


Figure 2: Shown on the left is a comparison between analytical derivatives and finite-difference approximation using different orders. Plotted are the absolute errors of the directional derivatives in a random direction. The right figure shows the convergence behavior for the steepest descent, a preconditioned steepest descent, and the BFGS quasi Newton algorithms for Problem I. Besides the evolution of the objective function, we show the max-norm of the part of the gradient with respect to the expansion axis ( $\|\nabla_{\mathbf{a}} J\|_{\infty}$ ) and the coil design parameters ( $\|\nabla_{\mathbf{c}} J\|_{\infty}$ ) during the BFGS iteration.

## 5. Problem I: A quasi-axisymmetric vacuum field with low rotational transform for electron-positron confinement

In this and the next section, we study the performance of gradient-based optimization algorithms for minimization of (9), reformulated as an unconstrained optimization of the form (12). We also study the optimization landscape, the influence of regularization, and properties of the obtained coil designs. In these sections, we set the constants  $s_{\psi} = s_G = 1$ .

As a first test, we solve (12) with regularization

$$R(\mathbf{c}, \mathbf{a}) := \frac{1}{2} \sum_{i=1}^{N_c} \left( \frac{L_c^{(i)}(\mathbf{c}) - L_{0,c}}{L_{0,c}} \right)^2 + \frac{1}{2} \left( \frac{L_a(\mathbf{a}) - L_{0,a}}{L_{0,a}} \right)^2, \quad (19)$$

and the target quantities

$$L_{c,0} = 0.7 \times 2\pi, \quad L_{a,0} = 2\pi, \quad \iota_{0,a} = 0.103, \quad (20)$$

where units of meters are assumed throughout. We use  $n_p^{\text{coil}} = n_p^{\text{axis}} = 9$ , and  $N_c = 4$ , initially flat, modular coils and apply 2-fold toroidal symmetry as well as stellarator symmetry. The coils are arranged uniformly on the initially flat axis as shown in Figures 5a, 5b, where the initial currents in the coils are zero, we fix the constant  $B_0 = 1$ , and use the initialization  $\bar{\eta} = 1$ . The target length of the coils and axis correspond to those in the initial configuration. Therefore, the regularization terms in (19) are initially zero. The target rotational transform is chosen as relatively small. Thus the desired  $\iota$  and quasisymmetry should be achievable to a good approximation with coils of moderate curvature. Since simple planar coil configurations easily yield near-perfect axisymmetry with  $\iota = 0$ , physical intuition suggests that achieving a small iota and quasisymmetry may not require a large curvature of the coils. High-performing stellarators typically have larger rotational transforms [13, 16, 20, 53], but the magnetic configuration we will obtain with this set-up of the optimization problem is relevant for experiments designed to confine and study electron-positron pair plasmas [42, 44]. For a low temperature pair plasma, with temperatures of the order of 1 electron-volt, confined in a relatively strong magnetic field, of the order of 1 or 2 Tesla, the drift of charged particles in a purely toroidal magnetic field is slow, because the particles are strongly magnetized. Therefore, a small amount of poloidal field, and a correspondingly small rotational transform is sufficient to provide the desired quality of confinement.



Mode #	$\sin x$	$\cos x$	$\sin y$	$\cos y$	$\sin z$	$\cos z$
0	-	1.0884e+00	-	2.2511e-01	-	2.6995e-02
1	-5.8491e-03	6.5503e-01	-2.8165e-02	1.2335e-01	6.2858e-01	-5.3515e-03
2	-8.0674e-03	3.9426e-02	9.8105e-02	3.0468e-02	3.5265e-02	-2.1969e-02
3	-2.3760e-03	4.1630e-02	-5.7865e-02	-7.1681e-03	1.6093e-02	8.6299e-04
4	1.9382e-03	-1.1647e-02	5.9301e-03	1.0502e-02	2.7819e-03	1.3789e-02
5	9.1377e-04	-5.2997e-03	1.2073e-02	1.2459e-03	8.0925e-03	5.7870e-03
6	-5.9186e-03	1.4024e-02	2.8668e-03	-2.0511e-03	3.1622e-03	-5.1570e-03
7	5.9704e-03	-1.0150e-02	-4.8427e-03	-8.0999e-03	-6.4598e-03	-7.1050e-03
8	-1.4711e-03	3.4307e-03	-3.0153e-03	7.3435e-03	2.1565e-03	3.0483e-03
9	-8.2496e-04	-7.6827e-04	-4.1981e-04	4.4477e-05	-9.8108e-04	2.3497e-03

Table 1: Fourier coefficients of the  $x$ ,  $y$ , and  $z$  expansions (5) associated to the first modular coil in the optimized configuration computed in Problem I.

### 5.1. Gradient-based optimization performance

We solve the stellarator optimization problem with various gradient-based methods, namely steepest descent with and without preconditioning, and a quasi-Newton method, which uses consecutive gradients to approximate the Hessian using the BFGS algorithm [36]. All methods use a cubic line search procedure to find an appropriate step length with sufficient decrease of the objective.

First, in the right plot of Figure 2 we compare the convergence of the steepest descent algorithms and the BFGS quasi-Newton method. For clarity of the figure, we only show the convergence for the norm of the gradient for the BFGS quasi-Newton methods. For the steepest descent method, we find that the objective function plateaus at  $(J, \|\nabla J\|_\infty) = (5.15 \times 10^{-1}, 4.47 \times 10^{-1})$ . Little progress is made over 4,000 iterations, which require 6,250 function and gradient evaluations. The excess function evaluations are due to the line search procedure. This slow convergence is due to the vastly different sensitivities of the objective with respect to the parameters, which we study in more detail in the next subsection. Improved convergence is obtained by multiplying the steepest descent direction with a preconditioning matrix that helps to balance these sensitivities. The preconditioning matrix we use is motivated by the sensitivity study in the next subsection and detailed there. The convergence history of the preconditioned gradient descent method seen on the right in Figure 2 shows that after 4,000 iterations and 6,199 function and gradient evaluations, we obtain  $(J, \|\nabla J\|_\infty) = (3.26 \times 10^{-5}, 1.12)$ . As can be seen, the norm of the gradient does not decrease substantially. However, the norm of the preconditioned gradient decreases by about 4 orders of magnitude, resulting in substantial decrease of the objective.

After 4,000 iterations of the quasi-Newton method, we have  $(J, \|\nabla J\|_\infty) = (1.54 \times 10^{-11}, 4.58 \times 10^{-6})$ . The resulting coil design is shown in Figures 5c, 5d and are discussed in section 5.3. These 4,000 iterations required 4,629 evaluations of  $J$  and its gradient, where the excess evaluations are again due to the line search procedure. From Figure 2 it can also be seen that the norm of the part of the gradient corresponding to the expansion axis,  $\nabla_{\mathbf{a}}J$ , dominates the norm of the part of the gradient corresponding to the coils  $\nabla_{\mathbf{c}}J$ . The much improved performance of the quasi-Newton algorithms as opposed to the steepest-descent algorithms shows that it is crucial for fast convergence to use second-order information.

Note that using a Fourier expansion with  $n_p^{\text{coil}} = 9$  modes is a modeling decision and has the advantage that the coils will be easier to manufacture than those with more modes. The Fourier coefficients of the first modular coil in the optimized configuration decay with increasing mode number (Table 1), typically by several orders of magnitude even though the objective in this example does not explicitly include regularization on coil curvature and torsion. Finally, in contrast to finite difference methods, enriching the coil parameter space does not directly increase the computational cost associated with calculating the gradient when using an adjoint approach, as done here.

### 5.2. Local study of optimization landscape

Next, we study the optimization landscape locally around the solution we found with the BFGS method. For convenience of notation, we denote the parameters for the coils and the expansion axis

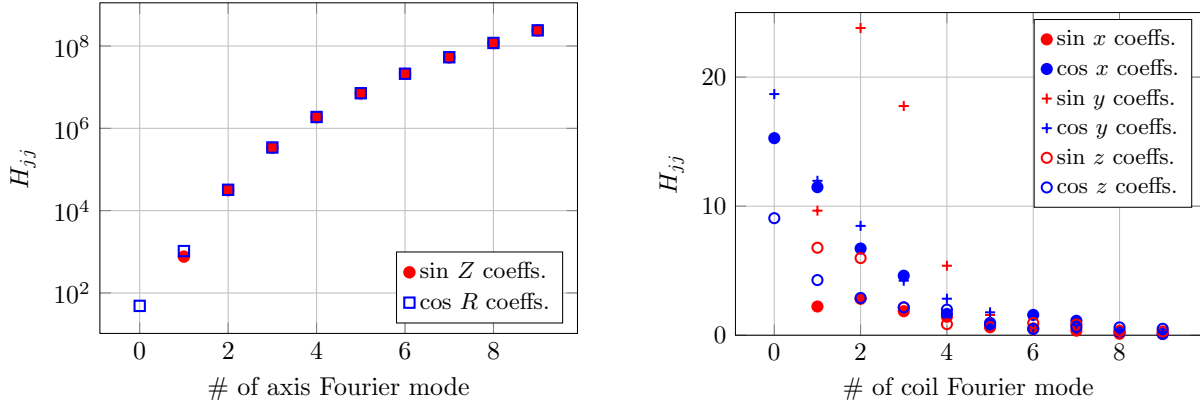


Figure 3: Hessian diagonal entries for Problem I: Shown on the left are the diagonal entries corresponding to the Fourier coefficients of the  $R$  and  $Z$  coordinates of the expansion axis. Shown on the right are the diagonal entries corresponding to the Fourier coefficients of the  $x$ ,  $y$  and  $z$ -coordinates of the first coil. For the expansion axis, the sensitivity of the objective grows with the mode number. For the coil, the sensitivity decreases with the mode number.

corresponding to this (approximate) minimum by  $\mathbf{x}^* := (\mathbf{c}^*, \mathbf{a}^*)$ . Since the gradient vanishes at  $\mathbf{x}^*$ , the objective function in the neighborhood of  $\mathbf{x}^*$  can be written as

$$J(\mathbf{x}^* + \mathbf{h}) = J(\mathbf{x}^*) + \frac{1}{2} \mathbf{h}^T H \mathbf{h} + \mathcal{O}(\|\mathbf{h}\|^3), \quad (21)$$

where  $H = \nabla^2 J(\mathbf{x}^*)$  is the Hessian of  $J$  at  $\mathbf{x}^*$ . This Taylor expansion shows that the local landscape of the objective around the minimizer is governed by properties of the Hessian matrix  $H$ . While we do not have direct access to second derivatives, we can approximate the application of  $H$  to a vector using finite differences of gradients. Applying  $H$  to unit vectors, we can thus construct an approximation to the Hessian matrix. Due to finite-difference errors, the approximate Hessian matrix constructed in this way would not be exactly symmetric. Thus, in the following we use the symmetrization  $\bar{H} := (\hat{H} + \hat{H}^T)/2$ , where  $\hat{H}$  is obtained using finite differences of gradients.

We first focus on the diagonal entries  $\bar{H}_{jj}$  of the Hessian  $\bar{H}$ . These entries describe how sensitive the objective is to the  $j$ th design parameter in a neighborhood of  $\mathbf{x}^*$ , which follows by choosing  $\mathbf{h} = \varepsilon \mathbf{e}_j$  in (21), where  $\mathbf{e}_j$  is the  $j$ th unit vector, and  $\varepsilon > 0$  is small. If  $\bar{H}_{jj}$  is large, then the objective function is very sensitive to variation of the  $j$ th design parameter. Alternatively, if  $\bar{H}_{jj}$  is small or even zero, the objective function is insensitive to variation in the  $j$ th design parameter. On the left in Figure 3, we show the diagonal entries of  $\bar{H}$  that correspond to the Fourier coefficients of the  $R$  and  $Z$ -coordinates of the expansion axis. Clearly, the objective is highly sensitive to the magnetic axis as the corresponding diagonal entries of  $\bar{H}$  range from  $\mathcal{O}(10^2)$  to  $\mathcal{O}(10^8)$ . Moreover, it can be seen that the objective is several orders of magnitude more sensitive to higher Fourier mode perturbations of the expansion axis than to low Fourier mode perturbations.

On the right in Figure 3, we show the diagonal entries of  $\bar{H}$  that correspond to the sine and cosine Fourier coefficients of the first coil's coordinates. Note that the objective function is not as sensitive to the coil parameters as it is to the expansion axis. Moreover, in contrast to what we found for the expansion axis,  $J$  is more sensitive to lower than to higher Fourier mode coil perturbations. This is due to the fact that only the evaluation of the magnetic field (and its gradient) at the expansion axis enter in the objective. Since the expansion axis is relatively far away from the coils and magnetic fields may cancel each other, higher Fourier modes in the coil representations have a smaller influence on the objective.

These different sensitivities result in extremely stretched contour lines of the objective around  $\mathbf{x}^*$ . This explains the slow convergence of the (un-preconditioned) steepest descent method [36] we observed

in subsection 5.1. Namely, the narrow valleys in the objective landscape result in small steps due to a behavior sometimes referred to as “zig-zagging” [36]. As discussed above, using a preconditioner improves the slow convergence of the steepest descent method. To illustrate this we used the inverse of a modified approximation of the Hessian as a preconditioning matrix for the results shown on the right in Figure 2. Specifically, we use the previously computed symmetrized finite difference approximation of the Hessian and modify it to be positive definite by adding the identity matrix  $(\bar{H} + I)^{-1}$ . Clearly, this preconditioner is not available in practice as the Hessian at the minimizer, and the minimizer itself, are not available. However, this experiment highlights that preconditioning is crucial for problems with extremely different parameter sensitivities. The quasi-Newton BFGS method that we use iteratively builds a Hessian approximation for preconditioning and thus significantly improves the convergence.

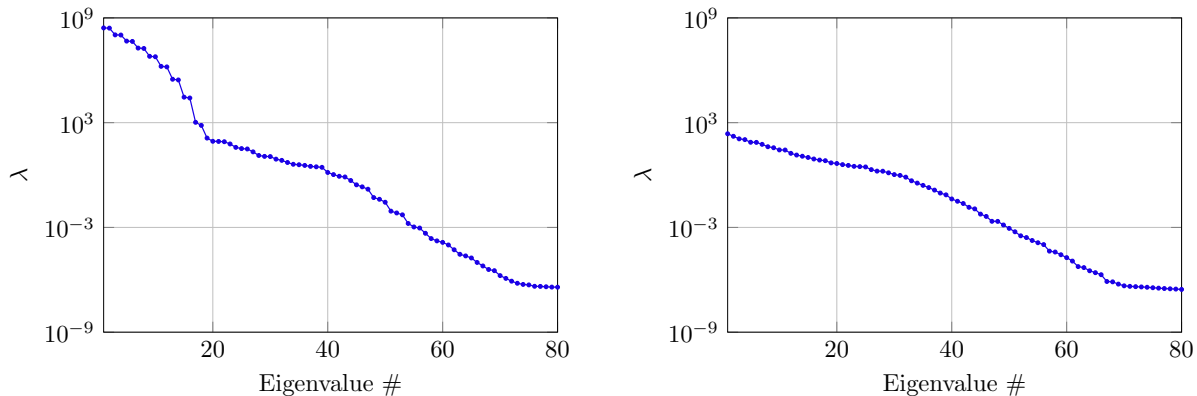


Figure 4: Hessian spectra for Problem I: Shown on the left are the largest (out of 252) eigenvalues of the Hessian approximation  $\bar{H}$ . The strong variation in eigenvalues results in extremely stretched contours of the objective and shows that the objective is mostly sensitive to perturbations in  $\sim 40$  parameter space directions, but mostly insensitive in other directions. Shown on the right are the largest (out of 228) eigenvalues of  $\bar{H}$  when the magnetic axis and coil currents are fixed. The large number of small eigenvalues indicate that we can introduce additional design constraints on the coils.

After studying sensitivities with respect to individual parameters, we now study the spectrum of the (approximate) Hessian  $\bar{H}$  at  $\mathbf{x}^*$ . At a minimizer, the Hessian must be positive semi-definite and the eigenvalues provide insight into the local geometry of the objective. In Figure 4 (left), we show the rapid decay of eigenvalues taking into account all 252 design parameters. In the right figure, we show the eigenvalues obtained when only considering the subspace of dimension 228 corresponding to the Fourier representation of the coil parameters. The large eigenvalues correspond to eigenvectors, i.e., directions in the parameter space, in which the objective has large curvature and thus is very sensitive to perturbations in these directions. Clearly, there are many directions in which the minimizer can be perturbed that do not substantially affect the value of the objective function. Some of these directions are due to the coil parametrization we use (section 3.1), while others indicate that there is substantial freedom to introduce additional design constraints on the coils or include coil manufacturing uncertainty, without changing the objective substantially. We examine this freedom in the next numerical example.

### 5.3. Discussion of coil designs

We now discuss the physical properties of the optimal solution obtained by the BFGS algorithm. In Figure 5, we show the initial and final coil configurations. The initially flat coils are uniformly arranged around the initially flat expansion axis (Figures 5a, 5b). From this initially axisymmetric configuration, the coils and axis reach a non-axisymmetric configuration where each individual term in the objective is nearly zero (Figures 5c, 5d).

We study the magnetic field generated by the optimized coils in two different ways. The first method is through Poincaré plots: starting at a large number of radial initial positions along the midplane  $Z = 0$

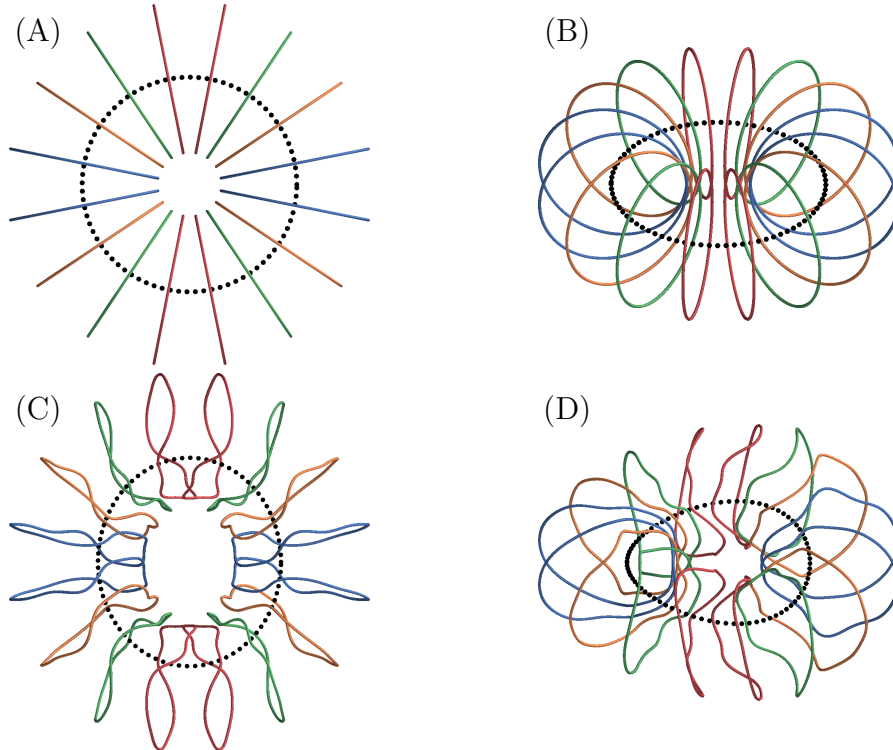


Figure 5: Initialization and optimized designs for Problem I: Shown are two views of the initial (upper row) and optimized (lower row) coils (in red, blue, green, magenta) and expansion axis (dotted black). Coils that correspond to the same modular coil after application of the symmetries are drawn in the same color. For the optimized setup, the expansion axis and the magnetic axis corresponding to the coils coincide.

at the toroidal angle  $\phi = 0$ , we numerically integrate the coupled ordinary differential equations to trace field lines, and compute their intersections with the plane  $\phi = 0$ , as well as the planes  $\phi = \pi/4$  and  $\phi = \pi/2$ . Poincaré plots give a visual indication of the existence of flux surfaces, which are closed toroidal surfaces on which the magnetic field is everywhere tangent to the surface, as well as the existence of magnetic islands and regions in which the magnetic field is chaotic. Large islands and chaotic magnetic field lines must be avoided in the plasma core to guarantee good confinement properties. Figure 6 demonstrates that our optimized coil configuration produces a vacuum magnetic field with nested toroidal flux surfaces over a large volume, and with no significant internal island chains. This is remarkable, since in our formulation of the optimization problem, we do not have terms which explicitly drive the optimum to a configuration with nested surfaces. We obtain a vacuum field with such a desirable property for at least two reasons: quasi-symmetric fields approximately constructed with the Garren-Boozer expansion are empirically found to have a large set of nested flux surfaces [30], and by focusing on a low value of the rotational transform, we avoid the large islands and chaotic magnetic fields which would be present at radii where the rotational transform is a low-order rational number [52].

Once the magnetic field lines have been constructed numerically, one can compute the field strength along the magnetic field lines, and obtain a first measure of the quality of the quasi-symmetry of the magnetic field produced by the coils obtained in our optimization. Indeed, the magnitude of a perfectly quasi-symmetric magnetic field is a periodic function along a magnetic field line [18], and only has a global maximum and a global minimum along a field line, and no local extrema. In the left of Figure 7, we plot the magnetic field strength along the fieldlines as a function of the toroidal angle for fieldlines close to the magnetic axis. This plot confirms that our optimization procedure led to coils corresponding

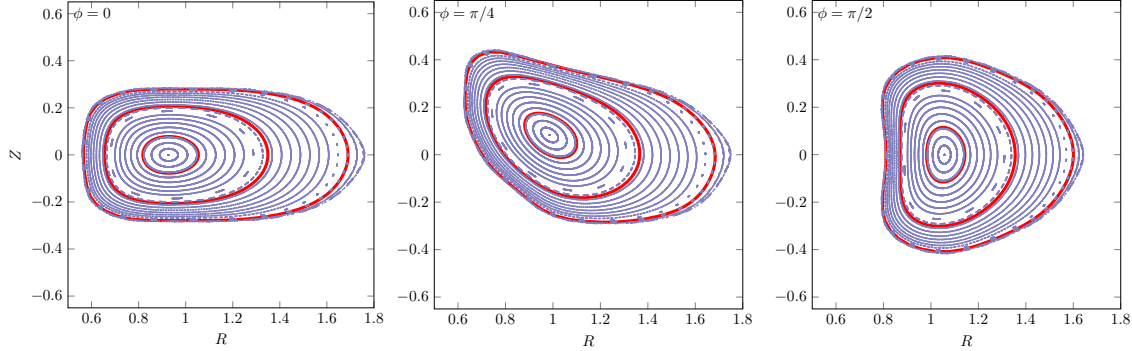


Figure 6: Poincaré plots for final design in Problem I. These plots are generated by following field lines around the origin and computing their intersection with the cylindrical angles  $\phi = 0, \pi/4,$  and  $\pi/2$ , shown as blue dots. The red lines correspond to the three surfaces plotted in Figure 8.

to a good approximation of a vacuum quasi-axisymmetric field close to the axis. The magnetic field strength along the field lines can be viewed as the sum of a periodic function with only global maxima and minima which line up for all the field lines, and a much smaller ripple with local minima and maxima. The amplitude of the ripple increases as one moves away from the magnetic axis, as one would expect from our formulation of the optimization problem, in which quasi-symmetry is only imposed on the expansion axis. We return to this observation shortly, from a slightly different viewpoint. To do so, we consider our second method of analyzing the vacuum field resulting from the coil optimization. It provides an alternative quantitative assessments of the quality of quasi-symmetry achieved.

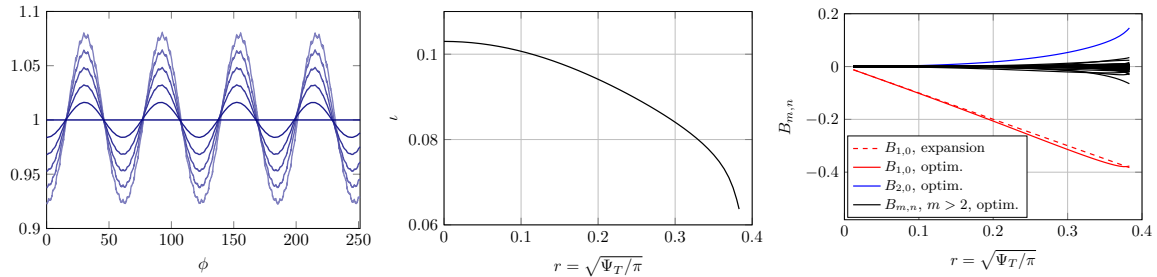


Figure 7: Results for the optimized stellarator in Problem I: Shown on the left is the field magnitude along fieldlines in the neighborhood of the magnetic axis. Shown in the middle is the rotational transform  $\nu$  as function of effective minor radius  $r$ . Shown on the right is the spectrum of the field magnitude  $B$  as function of  $r = \sqrt{\Phi_T/\pi}$ , where  $\Phi_T$  is the toroidal flux. Subscripts  $m$  and  $n$  on  $B$  refer to Fourier modes with respect to the Boozer poloidal and toroidal angle respectively.

When flux surfaces do exist, we can construct a numerical parameterization for them, as well as Boozer coordinates [3, 4] on each surface. Since the purpose of the present article is to focus on the formulation of the optimization problem, and the properties of the obtained optima, we will present our numerical scheme for doing so, as well as our method for computing the rotational transform on the surface, in a forthcoming article. The rotational transform profile is shown in the middle of Figure 7. As expected given our low target value  $\nu_{0,a} = 0.103$ , the rotational transform is small throughout the plasma volume. Furthermore, the radial variation of  $\nu$  is small. The coils we obtained thus generate what is called a “low-shear” vacuum magnetic field [52], where the  $\nu$  profile does not cross resonant values corresponding to low order rational numbers. As mentioned previously, this is one of the explanations for the fact that we have a large volume with nested flux surfaces, and do not have any island chains with large islands.

With the Boozer coordinates numerically constructed on each surface, we can compute the Fourier spectrum of the field strength. In the right plot of Figure 6, we show the radial profile of the Fourier modes  $B_{mn}$  of the field strength. The plot confirms that quasi-axisymmetry is achieved with very high accuracy in the neighborhood of the axis, and degrades as one moves away from the axis, which is consistent with theoretical results in the Garren-Boozer asymptotic analysis [30]. Throughout the plasma, the quasi-axisymmetric modes, with  $n = 0$ , have a much larger amplitude than the symmetry-breaking modes with  $n \neq 0$ .

Finally, for a perfectly quasi-axisymmetric field, the contours of constant magnitude of the magnetic field on a flux surface should be horizontal lines in Boozer coordinates [18]. We look at the degree to which our vacuum magnetic field satisfies this property by considering three different flux surfaces increasingly far from the magnetic axis. To visualize the radial location of the three surfaces, we highlighted them in the Poincaré plots in Figure 6. The first surface is in the neighborhood of the magnetic axis, the second surface is approximately at mid-radius, and the last surface is close to the last closed flux surface. In order to more quantitatively describe the distance of the three surfaces from the magnetic axis and the plasma volume enclosed by the flux surfaces, we define the aspect ratio of a flux surface as  $A := R_{\text{major}}/R_{\text{minor}}$ , where  $R_{\text{minor}}$  is the effective minor radius  $R_{\text{minor}} = \sqrt{\bar{A}/\pi}$ , with  $\bar{A}$  the average toroidal cross-sectional area of the surface, and  $R_{\text{major}}$  is the effective major radius  $R_{\text{major}} = V/(2\pi^2 R_{\text{minor}}^2)$ , where  $V$  the volume enclosed by the surface. The same definition of  $A$  is employed in the popular stellarator equilibrium code VMEC [21]. If the surface was a toroidally axisymmetric torus with a circular cross section, our definition of the aspect ratio would correspond to the intuitive definition of the ratio of the major radius to the minor radius. In Figure 8, we show the three magnetic surfaces mentioned before which have decreasing aspect ratios of 10.43, 3.85, and 2.84, together with the optimized coil system. An aspect ratio of 2.84 is quite low as compared to current stellarator experiments and recent designs of new machines, and corresponds to a compact magnetic configuration, which can be desirable regarding cost of construction. In agreement with Figure 7, on the surfaces close to the axis, we observe a good approximation to quasi-axisymmetry, with field strengths which almost exclusively vary with the Boozer poloidal angle  $\theta$ . For surfaces further away from the axis, the discrete nature of the coils becomes apparent and the quality of the quasi-axisymmetry degrades. Since we are only optimizing for near-axis quasi-symmetry, this motivates an off-axis optimization of quasi-symmetry, which will be the subject of future research.

## 6. Problem II: Optimizing the nonplanar coils of the National Compact Stellarator Experiment (NCSX)

We consider a second example that is inspired by the coil configuration of the National Compact Stellarator Experiment (NCSX). NCSX is a compact high performance stellarator with quasi-axisymmetry which was designed in the 1990s and early 2000s [39, 53]. NCSX was partially built but the project was cancelled in 2008, because the estimated cost and schedule for completing the project grew as the technical requirements and risks became better understood [35]. The NCSX stellarator is composed of three unique modular coil shapes to which stellarator symmetry and three-fold toroidal symmetry are applied. The NCSX design also included planar toroidal field coils and poloidal field coils, which are not included in our study for simplicity. Thus, we consider a total of 18 coils in our optimization for near-axis quasi-symmetry. Since we ignore NCSX's poloidal and planar toroidal field coils, and we consider the case of no plasma current, our configuration is not directly comparable to the complete NCSX design on which the construction of the experiment was based. However we can still expect the NCSX coil shapes to provide an initial condition in an interesting region of parameter space, as an alternative to the planar circular shapes used to initialize Problem I.

The initial coil geometries use the first  $n_p^{\text{coil}} = 6$  Fourier modes of the NCSX modular coils, and the expansion axis geometry uses  $n_p^{\text{axis}} = 4$  Fourier modes. Our target rotational transform, axis length, and coil lengths are set to coincide with the corresponding values for the original NCSX non-planar coil

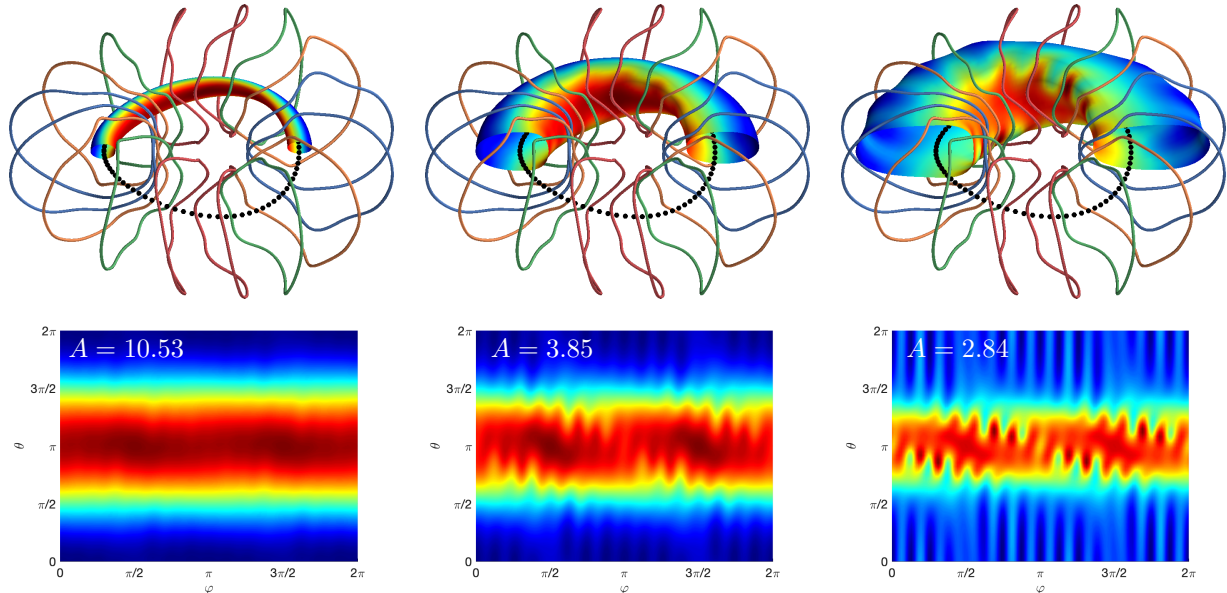


Figure 8: Surfaces corresponding to different aspect ratios  $A$  (upper row) and field strength on these surfaces (lower row) for the optimized stellarator of Problem I. In the lower row, the axes  $\theta$  and  $\varphi$  are the Boozer poloidal and toroidal angles. Hot colors on the surface correspond to high field strength and cold colors correspond to low field strength. Color scales are different between columns. Perfect quasi-axisymmetry on the surfaces corresponds to field strengths that only vary with  $\theta$ . On surfaces close to the coils, we observe the field strength variations caused by the coils, indicating a degraded approximation of quasi-axisymmetry.

shapes with their original currents, i.e.,

$$\iota_{0,a} = 0.395939, \quad L_{0,c}^{(1)} = 6.851923, \quad L_{0,c}^{(2)} = 6.480790, \quad L_{0,c}^{(3)} = 5.816940, \quad L_{0,a} = 9.421513.$$

We divide the NCSX coil currents by the mean field strength on the magnetic axis of the initial configuration, 1.474, since we fix  $B_0 = 1$ . Moreover, we set  $s_\psi = s_G = 1$  and choose the initial guess  $\bar{\eta} = 0.685$  since this results in an initial quasi-symmetric rotational transform close to the target value  $\iota_{0,a}$ .

We present solutions of (11) with different coil regularization parameters. Namely, we use regularizations of the following form

$$R(\mathbf{c}, \mathbf{a}) := \sum_{i=1}^{N_c} \left[ \frac{1}{2} \left( \frac{L_{i,c}(\mathbf{c}) - L_{0,c}}{L_{0,c}} \right)^2 + \frac{\delta}{4} k_i(\mathbf{c}) + \frac{\gamma}{2} \sum_{j=1}^{i-1} d_{i,j}(\mathbf{c}) \right] + \frac{1}{2} \left( \frac{L_a(\mathbf{a}) - L_{0,a}}{L_{0,a}} \right)^2, \quad (22)$$

and consider three cases to study the effect of different regularization choices. First, for finding design (II.A), we only use length penalties on the coils and the expansion axis, i.e., we set  $\delta = \gamma = 0$ . For the design (II.B), we add the minimum distance penalty, i.e.,  $\delta = 0$ ,  $\gamma = 2000$ ,  $d_{\min} = 0.2$ . Finally, to compute the design (II.C), we additionally add a curvature penalty by setting  $\delta = 4 \times 10^{-6}$ ,  $\gamma = 2000$ ,  $d_{\min} = 0.2$ . The weights multiplying the penalty terms are chosen by trial-and-error, to ensure that the physics penalty terms are not overpowered by the regularization terms.

As can be seen in Figure 9, compared to the initial coils (II.Init), the design (II.A) yields a much better approximation of quasi-axisymmetry near the expansion axis. However, the coils are irregularly shaped and quite close to one another—they even interweave with each other. In fact, the coil distance is less than 0.022 in some locations. This motivates introducing the minimum distance term in the regularization to compute design (II.B). Doing so successfully prevents the coils from becoming too close to one another, with the minimum distance now approximately 0.2, as we show in the lower left of



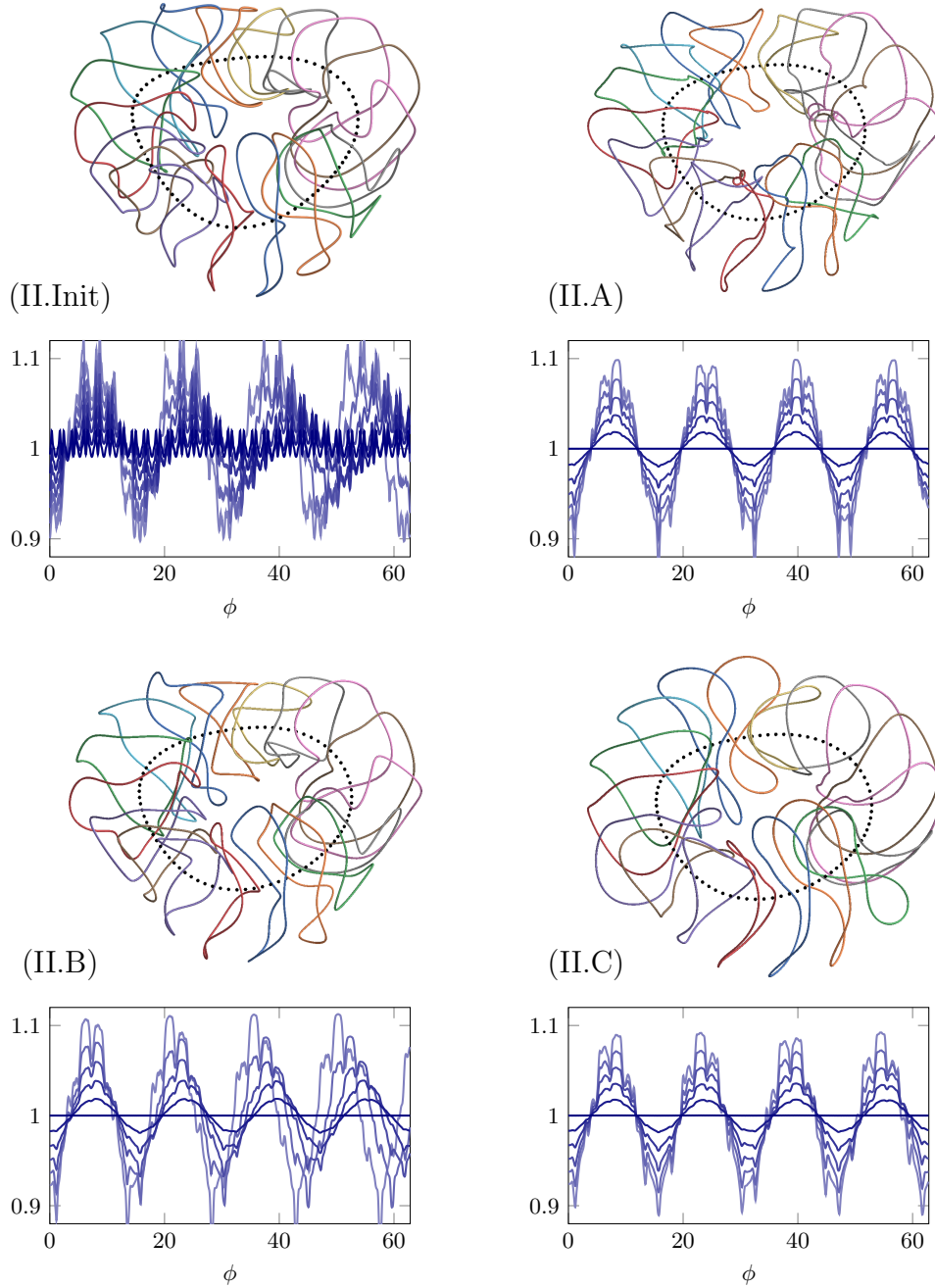


Figure 9: Designs for Problem II: Shown are the coils and field strength along field lines for initial configuration and from optimization with different coil regularizations. The initial coils are denoted by (II.Init), coils (II.A) are obtained with only coil and axis length regularization, coils (II.B) are obtained with additional minimum distance regularization, and coils (II.C) are obtained with additional curvature regularization.



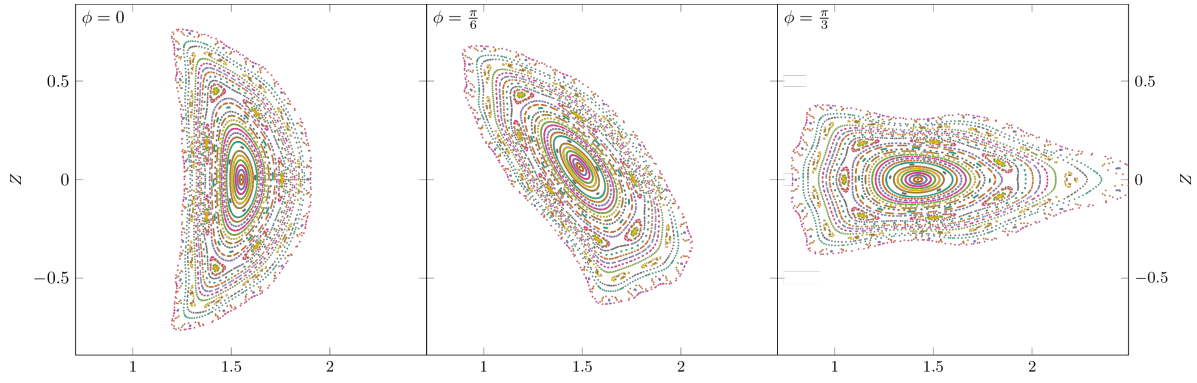


Figure 10: Poincaré plots for Problem II.C with minimum distance and curvature regularization terms. These plots are generated by following field lines around the origin and computing their intersection with the cylindrical angles  $\phi = 0$ ,  $\pi/6$ , and  $\pi/3$ , shown as dots. Points of intersection belonging to the same field line are plotted with the same color.

Figure 9. However, the maximum curvature of the coils in design (II.A) is 22.79 and is 26.76 with the additional penalty term in design (II.B). In order to address this issue, we introduce the maximum curvature term in the regularization, which produces design (II.C). The lower right of Figure 9 shows that design (II.C) has smooth and well-behaved coils, with maximum curvature of just 2.29. We note that introducing the additional penalty terms for designs (II.B) and (II.C) does not substantially degrade the quasi-axisymmetry in the neighborhood of the expansion axis, as can be seen in the bottom of Figure 9. This is a consequence of the many directions in parameter space in which the quasi-symmetry remains nearly unchanged as observed in Problem I, resulting in substantial freedom for the coils while maintaining good confinement properties.

Poincaré plots are provided for design (II.C). They show the existence of magnetic surfaces with low aspect ratio, and the existence of a few wider island chains compared to Problem 1. We again plot the eigenvalues of the Hessian at minimizers in Figure 11. We show the spectrum for all design parameters (axis, coils and current) and the spectrum for the part of the Hessian corresponding to the geometric coil parameters only. For (II.A), the overall spectrum varies over more than 12 orders of magnitude, with a large number of small eigenvalues. These small eigenvalues mean that the optimizer can be perturbed in many directions with little impact on the objective to second order. For (II.B), obtained with the minimum distance constraint, the optimal coils have a minimum pairwise distance of 0.199999. This value is quite close to the target minimal distance  $d_{\min} = 0.2$  since we chose a large penalty parameter  $\gamma$ . This distance constraint increases most of the small Hessian eigenvalues to at least  $10^{-4}$ . Finally, for (II.C), obtained with an additional curvature regularization, most eigenvalues are increased to  $10^{-3}$ . This shows that adding constraints increases the curvature of the Hessian at the minimizer and thus has a (local) convexification effect on the minimization landscape, in particular in the mostly flat directions. Such regularization does not lead to considerable degradation of confinement properties of the stellarator but helps to identify coils that are simpler and thus more cost-effective to manufacture.

## 7. Conclusions and perspective

We have presented a new approach to coil design, where we directly optimize stellarator coils for quasi-symmetry on an expansion axis. We relied on gradient-based optimization algorithms, for which we computed exact derivatives of the objective function using either the forward sensitivity or the adjoint method. Both methods yield more accurate derivatives and are substantially less computationally expensive than evaluating derivatives through numerical finite differences. We have applied our new formulation to design two configurations of physical interest. The first application is a compact vac-

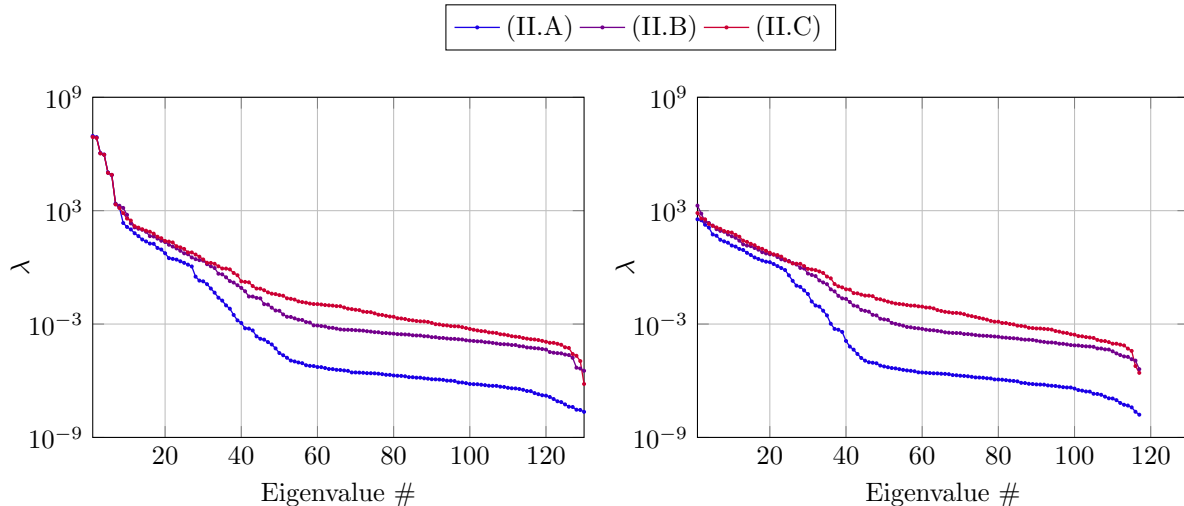


Figure 11: Hessian spectra for Problem II: Shown on the left are the eigenvalues of the Hessian at the minimizers for designs (II.A), (II.B) and (II.C) characterized by different regularization parameters for Problem II as explained in section 6. Shown on the right are the eigenvalues of the Hessian when the magnetic axis and coil currents are fixed.

uum quasi-axisymmetric magnetic field which could be suitable for the confinement of a low-density electron-positron plasma. The second application is a simplification of the non-planar coils of the NCSX experiment, targeting good vacuum quasi-axisymmetry. In both problems, we showed that our method worked in a satisfactory manner, leading to a good approximation of quasi-axisymmetry, and the existence of nested flux surfaces for a large plasma volume. By analyzing the optimization landscape locally around the optimal solutions, we observed that there is substantial freedom in imposing design constraints on the coils, corresponding to the many directions in which the minimizer can be perturbed that do not substantially affect the value of the objective. In our numerical tests, we also find that using an optimization method that incorporates approximate second-order derivative information, such as the BFGS method, is crucial for numerical convergence.

Our results motivate the future use of single-stage optimization for the detailed design of new stellarator experiments. Our method is directly applicable to other quasi-symmetries, particularly the also attractive quasi-helical symmetry, which also fit in the Garren-Boozer near-axis expansion framework. However, for complete design studies, our method needs to be extended in several directions before it can be widely used. We need to develop a robust method to ensure good quasi-symmetry throughout the plasma for confinement, and not just near the magnetic axis. For that purpose, we are currently exploring the idea of including a term driving off-axis quasi-symmetry in the objective. Our single-stage approach also lends itself toward incorporating coil manufacturing errors into the design process, resulting in stochastic stellarator optimization. Recently results in this direction show that incorporating such stochasticity reduces the occurrence of local minimizers and near-flatness of the objective in some directions [50]. In addition, in stellarators designed for magnetic confinement fusion research, plasma pressure is sufficiently high that the magnetic field is not well approximated by a vacuum field. We thus need to generalize our approach to apply it to finite-pressure magnetic configurations. This can be done in several ways. One way is to consider higher-order terms in the Garren-Boozer asymptotic expansion, which contain the modifications to the magnetic field due to the plasma pressure. Another way, which has the advantage of not being restricted to quasi-symmetric configurations, is to couple our method with a solver that computes the magnetic field accounting for the plasma pressure starting from the geometry of the coils and their currents, i.e. a “free-boundary” equilibrium solver, as it is called in the magnetic confinement fusion community. Finally, for detailed stellarator designs, the objective must include many more terms corresponding to additional physics and engineering goals, such as the mini-

mization of turbulent transport, or the loss of energetic particles. Such terms typically involve complex models and equations, and analytical derivatives would likely be complicated to obtain. Automatic differentiation could then be a promising approach to compute exact derivatives and avoid the limitations of finite differences for the evaluation of the gradients, as was shown recently for stellarator coil design with the two-stage method [32]. All these questions are the subject of ongoing research, with progress to be reported in the future.

## Acknowledgements

This research was supported by the Simons Foundation/SFARI (560651, AB). AC was additionally supported by the U.S. Department of Energy, Office of Science, Fusion Energy Sciences under Awards No. DE-FG02-86ER53223 and DE-SC0012398. GS was additionally supported by the US National Science Foundation under Award No. DMS-1723211. AG was additionally supported by the Natural Sciences and Engineering Research Council of Canada (NSERC) postdoctoral fellowship.

## Code availability

For reproducibility, we provide the code used to generate the examples presented in this paper. The code for the first example can be found at

<https://github.com/andrewgiuliani/matplasmaopt.git>

The code for the second example can be found under

<https://github.com/florianwechsung/PyPlasma0pt/releases/tag/v1.0.0>

and was archived on Zenodo at [49].

## Appendix A. Jacobian of the discrete state equation

We recall that the discrete state equation is (8). The components of  $\partial \mathbf{g} / \partial \boldsymbol{\sigma}$  are

$$\begin{aligned} \frac{\partial g_i}{\partial \sigma_j} &= \frac{|G_0|}{\ell'_i B_0} D_{i,j} + 2\iota \delta_{i-j} \sigma_i & 0 \leq i, j \leq n_\phi - 1, \\ \frac{\partial g_{n_\phi}}{\partial \sigma_j} &= 0 & 1 \leq j \leq n_\phi - 1, \\ \frac{\partial g_{n_\phi}}{\partial \sigma_0} &= 1, \end{aligned}$$

where  $\delta_{i-j}$  is the Kronecker delta. The components of  $\partial \mathbf{g} / \partial \iota$  are

$$\begin{aligned} \frac{\partial g_i}{\partial \iota} &= \frac{\bar{\eta}^4}{\kappa_i^4} + 1 + \sigma_i^2 & 0 \leq i \leq n_\phi - 1, \\ \frac{\partial g_{n_\phi}}{\partial \iota} &= 0. \end{aligned}$$

## Appendix B. Derivatives of discrete objective

We recall that the discretized objective function is (9). The components of  $\partial\hat{J}/\partial c_i$  and  $\partial\hat{J}/\partial a_i$  are

$$\begin{aligned}\frac{\partial\hat{J}}{\partial c_i} &= \left(\frac{2\pi}{n_\phi}\right) \left\{ \sum_{q=0}^{n_\phi-1} \left[ \sum_{j=1,2,3} (B_{\text{coils},q}^j - B_{\text{QS},q}^j) \frac{\partial}{\partial c_i} B_{\text{coils},q}^j \right. \right. \\ &\quad \left. \left. + \sum_{j=1,2,3} \sum_{k=1,2,3} (\nabla_k B_{\text{coils},q}^j - \nabla_k B_{\text{QS},q}^j) \frac{\partial}{\partial c_i} \nabla_k B_{\text{coils},q}^j \right] \|\Gamma'(\phi_q)\| \right\} + \frac{\partial}{\partial c_i} R(\mathbf{c}, \mathbf{a}), \\ \frac{\partial\hat{J}}{\partial a_i} &= \left(\frac{2\pi}{n_\phi}\right) \left\{ \sum_{q=0}^{n_\phi-1} \left[ \sum_{j=1,2,3} (B_{\text{coils},q}^j - B_{\text{QS},q}^j) \frac{\partial}{\partial a_i} (B_{\text{coils},q}^j - B_{\text{QS},q}^j) \right. \right. \\ &\quad \left. \left. + \sum_{j=1,2,3} \sum_{k=1,2,3} (\nabla_k B_{\text{coils},q}^j - \nabla_k B_{\text{QS},q}^j) \frac{\partial}{\partial a_i} (\nabla_k B_{\text{coils},q}^j - \nabla_k B_{\text{QS},q}^j) \right] \|\Gamma'(\phi_q)\| \right. \\ &\quad \left. + \left[ \frac{1}{2} \|\mathbf{B}_{\text{coils},q}(\mathbf{c}) - \mathbf{B}_{\text{QS},q}(\mathbf{a})\|^2 + \frac{1}{2} \|\nabla \mathbf{B}_{\text{coils},q}(\mathbf{c}) - \nabla \mathbf{B}_{\text{QS},q}(\mathbf{a}, \boldsymbol{\sigma}, \iota)\|^2 \right] \frac{\partial}{\partial a_i} \|\Gamma'(\phi_q)\| \right\} \\ &\quad + \frac{\partial}{\partial a_i} R(\mathbf{c}, \mathbf{a}),\end{aligned}$$

where  $\nabla_k B_{\text{QS}}^j$ ,  $\nabla_k B_{\text{coils}}^j$  are the  $k$ th component of the gradient in the  $j$ th Cartesian component of the magnetic field from the quasi-symmetric expansions and the one generated by the coils, respectively. The components of  $\partial\hat{J}/\partial \boldsymbol{\sigma}$ , and  $\partial\hat{J}/\partial \iota$  are

$$\begin{aligned}\frac{\partial\hat{J}}{\partial \sigma_i} &= \left(\frac{2\pi}{n_\phi}\right) \sum_{q=0}^{n_\phi-1} \left\{ \sum_{j=1,2,3} \sum_{k=1,2,3} (\nabla_k B_{\text{QS},q}^j - \nabla_k B_{\text{coils},q}^j) \frac{\partial \nabla_k B_{\text{QS},q}^j}{\partial \sigma_i} \|\Gamma_{\mathbf{a}}(\phi_q)\| \right\}, \\ \frac{\partial\hat{J}}{\partial \iota} &= \frac{1}{\iota_{0,a}^2} (\iota - \iota_{0,a}) + \left(\frac{2\pi}{n_\phi}\right) \sum_{q=0}^{n_\phi-1} \left\{ \sum_{j=1,2,3} \sum_{k=1,2,3} (\nabla_k B_{\text{QS},q}^j - \nabla_k B_{\text{coils},q}^j) \frac{\partial \nabla_k B_{\text{QS},q}^j}{\partial \iota} \|\Gamma_{\mathbf{a}}(\phi_q)\| \right\}.\end{aligned}$$

## References

- [1] Bader, A., Faber, B.J., Schmitt, J.C., Anderson, D.T., Drevlak, M., Duff, J.M., Frerichs, H., Hegna, C.C., Kruger, T.G., Landreman, M., McKinney, I.J., Singh, L., Schroeder, J.M., Terry, P.W., Ware, A.S., 2020. A new optimized quasisymmetric stellarator. [arXiv:2004.11426](https://arxiv.org/abs/2004.11426).
- [2] Bader, A., Kruger, T., 2020. Ensuring equilibrium evaluations do not depend on parametrization. Presentation in Wisconsin Optimized Stellarator Project Group Meetings.
- [3] Boozer, A.H., 1981a. Establishment of magnetic coordinates for a given magnetic field. Technical Report. Princeton Univ., NJ (USA). Plasma Physics Lab.
- [4] Boozer, A.H., 1981b. Plasma equilibrium with rational magnetic surfaces. *The Physics of Fluids* 24, 1999–2003. URL: <https://aip.scitation.org/doi/abs/10.1063/1.863297>, doi:10.1063/1.863297, [arXiv:https://aip.scitation.org/doi/pdf/10.1063/1.863297](https://aip.scitation.org/doi/pdf/10.1063/1.863297).
- [5] Boozer, A.H., 1995. Quasi-helical symmetry in stellarators. *Plasma Physics and Controlled Fusion* 37, A103–A117. doi:10.1088/0741-3335/37/11a/007.
- [6] Boozer, A.H., 1998. What is a stellarator? *Physics of Plasmas* 5, 1647–1655. doi:10.1063/1.872833.
- [7] Borzì, A., Schulz, V., 2012. Computational Optimization of Systems Governed by Partial Differential Equations. SIAM.

- [8] Brown, T., Breslau, J., Gates, D., Pomphrey, N., Zolfaghari, A., 2015. Engineering optimization of stellarator coils lead to improvements in device maintenance, in: 2015 IEEE 26th Symposium on Fusion Engineering (SOFE), pp. 1–6.
- [9] Canik, J.M., Anderson, D.T., Anderson, F.S.B., Likin, K.M., Talmadge, J.N., Zhai, K., 2007. Experimental demonstration of improved neoclassical transport with quasihelical symmetry. *Phys. Rev. Lett.* 98, 085002. doi:10.1103/PhysRevLett.98.085002.
- [10] Conn, A.R., Scheinberg, K., Vicente, L.N., 2009. Introduction to derivative-free optimization. SIAM.
- [11] Dewar, R., Hudson, S., 1998. Stellarator symmetry. *Physica D: Nonlinear Phenomena* 112, 275–280. doi:[https://doi.org/10.1016/S0167-2789\(97\)00216-9](https://doi.org/10.1016/S0167-2789(97)00216-9). proceedings of the Workshop on Time-Reversal Symmetry in Dynamical Systems.
- [12] Drevlak, M., 1998. Automated optimization of stellarator coils. *Fusion Technology* 33, 106–117. doi:10.13182/FST98-A21.
- [13] Drevlak, M., Brochard, F., Helander, P., Kisslinger, J., Mikhailov, M., Nührenberg, C., Nührenberg, J., Turkin, Y., 2013. Estell: A quasi-toroidally symmetric stellarator. *Contributions to Plasma Physics* 53, 459–468. doi:10.1002/ctpp.201200055.
- [14] Garabedian, P.R., 2008. Three-dimensional analysis of tokamaks and stellarators. *Proceedings of the National Academy of Sciences* 105, 13716–13719. URL: <https://www.pnas.org/content/105/37/13716>, doi:10.1073/pnas.0806354105.
- [15] Garren, D.A., Boozer, A.H., 1991. Existence of quasihelically symmetric stellarators. *Physics of Fluids B: Plasma Physics* 3, 2822–2834. URL: <https://doi.org/10.1063/1.859916>, doi:10.1063/1.859916.
- [16] Geiger, J., Beidler, C.D., Feng, Y., Maaßberg, H., Marushchenko, N.B., Turkin, Y., 2014. Physics in the magnetic configuration space of W7-X. *Plasma Physics and Controlled Fusion* 57, 014004. doi:10.1088/0741-3335/57/1/014004.
- [17] Gunzburger, M.D., 2003. *Perspectives in Flow Control and Optimization*. SIAM, Philadelphia.
- [18] Helander, P., 2014. Theory of plasma confinement in non-axisymmetric magnetic fields. *Reports on Progress in Physics* 77, 087001. doi:10.1088/0034-4885/77/8/087001.
- [19] Helander, P., Beidler, C.D., Bird, T.M., Drevlak, M., Feng, Y., Hatzky, R., Jenko, F., Kleiber, R., Proll, J.H.E., Turkin, Y., Xanthopoulos, P., 2012. Stellarator and tokamak plasmas: a comparison. *Plasma Physics and Controlled Fusion* 54, 124009. doi:10.1088/0741-3335/54/12/124009.
- [20] Henneberg, S., Drevlak, M., Nührenberg, C., Beidler, C., Turkin, Y., Loizu, J., Helander, P., 2019. Properties of a new quasi-axisymmetric configuration. *Nuclear Fusion* 59, 026014. doi:10.1088/1741-4326/aaf604.
- [21] Hirshman, S., van Rij, W., Merkel, P., 1986. Three-dimensional free boundary calculations using a spectral green’s function method. *Computer Physics Communications* 43, 143 – 155. doi:[https://doi.org/10.1016/0010-4655\(86\)90058-5](https://doi.org/10.1016/0010-4655(86)90058-5).
- [22] Imbert-Gerard, L.M., Paul, E.J., Wright, A.M., 2020. An introduction to stellarators: From magnetic fields to symmetries and optimization. *arXiv:1908.05360*.
- [23] Jackson, J.D., 1999. *Classical electrodynamics*. 3rd ed. ed., Wiley, New York, NY. URL: <http://cdsweb.cern.ch/record/490457>.

- [24] Klinger, T., Baylard, C., Beidler, C., Boscary, J., Bosch, H., Dinklage, A., Hartmann, D., Helander, P., Maßberg, H., Peacock, A., Pedersen, T., Rummel, T., Schauer, F., Wegener, L., Wolf, R., 2013. Towards assembly completion and preparation of experimental campaigns of Wendelstein 7-X in the perspective of a path to a stellarator fusion power plant. *Fusion Engineering and Design* 88, 461 – 465. doi:<https://doi.org/10.1016/j.fusengdes.2013.02.153>. proceedings of the 27th Symposium On Fusion Technology (SOFT-27); Liège, Belgium, September 24-28, 2012.
- [25] Ku, L.P., Garabedian, P.R., Lyon, J., Turnbull, A., Grossman, A., Mau, T.K., Zarnstorff, M., Team, A., 2008. Physics design for ARIES-CS. *Fusion Science and Technology* 54, 673–693. URL: <https://doi.org/10.13182/FST08-A1899>, doi:10.13182/FST08-A1899.
- [26] Landreman, M., 2017. An improved current potential method for fast computation of stellarator coil shapes. *Nuclear Fusion* 57, 046003. doi:10.1088/1741-4326/aa57d4.
- [27] Landreman, M., 2021. Figures of merit for stellarators near the magnetic axis. *Journal of Plasma Physics* 87, 905870112. doi:10.1017/S0022377820001658.
- [28] Landreman, M., Sengupta, W., 2018. Direct construction of optimized stellarator shapes. Part 1. Theory in cylindrical coordinates. *Journal of Plasma Physics* 84, 905840616. doi:10.1017/S0022377818001289.
- [29] Landreman, M., Sengupta, W., 2019. Constructing stellarators with quasisymmetry to high order. *Journal of Plasma Physics* 85.
- [30] Landreman, M., Sengupta, W., Plunk, G.G., 2019. Direct construction of optimized stellarator shapes. Part 2. Numerical quasisymmetric solutions. *Journal of Plasma Physics* 85, 905850103. doi:10.1017/S0022377818001344.
- [31] Liu, H., Shimizu, A., Isobe, M., Okamura, S., Nishimura, S., Suzuki, C., Xu, Y., Zhang, X., Liu, B., Huang, J., Wang, X., Liu, H., Tang, C., Yin, D., Wan, Y., team, C., 2018. Magnetic configuration and modular coil design for the chinese first quasi-axisymmetric stellarator. *Plasma and Fusion Research* 13, 3405067–3405067. doi:10.1585/pfr.13.3405067.
- [32] McGreivy, N., Hudson, S.R., Zhu, C., 2020. Optimized finite-build stellarator coils using automatic differentiation. *arXiv:2009.00196*.
- [33] Merkel, P., 1987. Solution of stellarator boundary value problems with external currents. *Nuclear Fusion* 27, 867–871. doi:10.1088/0029-5515/27/5/018.
- [34] Mynick, H.E., Pomphrey, N., Xanthopoulos, P., 2010. Optimizing stellarators for turbulent transport. *Phys. Rev. Lett.* 105, 095004. doi:10.1103/PhysRevLett.105.095004.
- [35] Neilson, G.H., Gruber, C.O., Harris, J.H., Rej, D.J., Simmons, R.T., Strykowski, R.L., 2010. Lessons learned in risk management on NCSX. *IEEE Transactions on Plasma Science* 38, 320–327.
- [36] Nocedal, J., Wright, S.J., 2006. *Numerical Optimization*. second ed., Springer Verlag, Berlin, Heidelberg, New York.
- [37] Nührenberg, J., Zille, R., 1988. Quasi-helically symmetric toroidal stellarators. *Physics Letters A* 129, 113–117. doi:[https://doi.org/10.1016/0375-9601\(88\)90080-1](https://doi.org/10.1016/0375-9601(88)90080-1).
- [38] Paul, E., Landreman, M., Bader, A., Dorland, W., 2018. An adjoint method for gradient-based optimization of stellarator coil shapes. *Nuclear Fusion* 58, 076015. doi:10.1088/1741-4326/aac1c7.

- [39] Reiman, A., Ku, L., Monticello, D., Hirshman, S., Hudson, S., Kessel, C., Lazarus, E., Mikkelsen, D., Zarnstorff, M., Berry, L.A., Boozer, A., Brooks, A., Cooper, W.A., Drevlak, M., Fredrickson, E., Fu, G., Goldston, R., Hatcher, R., Isaev, M., Jun, C., Knowlton, S., Lewandowski, J., Lin, Z., Lyon, J.F., Merkel, P., Mikhailov, M., Miner, W., Mynick, H., Neilson, G., Nelson, B.E., Nührenberg, C., Pomphrey, N., Redi, M., Reiersen, W., Rutherford, P., Sanchez, R., Schmidt, J., Spong, D., Strickler, D., Subbotin, A., Valanju, P., White, R., 2001. Recent advances in the design of quasiaxisymmetric stellarator plasma configurations. *Physics of Plasmas* 8, 2083–2094. URL: <https://doi.org/10.1063/1.1351826>, doi:10.1063/1.1351826.
- [40] De los Reyes, J.C., 2015. Numerical PDE-constrained optimization. Springer.
- [41] Seiwald, B., Kasilov, S., Kernbichler, W., Kalyuzhnyj, V., Nemov, V., Tribaldos, V., Jiménez, J., 2008. Optimization of energy confinement in the  $1/\nu$  regime for stellarators. *Journal of Computational Physics* 227, 6165 – 6183. URL: <http://www.sciencedirect.com/science/article/pii/S0021999108001265>, doi:<https://doi.org/10.1016/j.jcp.2008.02.026>.
- [42] Stenson, E., 2019. Plans for epos: A tabletop-sized, superconducting, optimized stellarator for matter/antimatter pair plasmas. *Stellarator News* 167, 5 – 8.
- [43] Stewart, J., 2012. Essential calculus: Early transcendentals. Cengage Learning.
- [44] Stoneking, M., Pedersen, T., Helander, P., Chen, H., Hergenbahn, U., Stenson, E., Fiksel, G., von der Linden, J., Saitoh, H., Surko, C., Danielson, J., Hugenschmidt, C., Horn-Stanja, J., Mishchenko, A., Kennedy, D., Deller, A., Card, A., Nissl, S., Singer, M., Singer, M., Koenig, S., Willingale, L., Peebles, J., Edwards, M., Chin, K., 2020. A new frontier in laboratory physics: magnetized electron-positron plasmas. *Journal of Plasma Physics* , Accepted for publication.
- [45] Strickler, D.J., Berry, L.A., Hirshman, S.P., 2002. Designing coils for compact stellarators. *Fusion Science and Technology* 41, 107–115. doi:10.13182/FST02-A206.
- [46] Strickler, D.J., Hirshman, S.P., Spong, D.A., Cole, M.J., Lyon, J.F., Nelson, B.E., Williamson, D.E., Ware, A.S., 2004. Development of a robust quasi-poloidal compact stellarator. *Fusion Science and Technology* 45, 15–26. doi:10.13182/FST04-A421.
- [47] Strykowsky, R.L., Brown, T., Chrzanowski, J., Cole, M., Heitzenroeder, P., Neilson, G.H., Rej, D., Viol, M., 2009. Engineering cost schedule lessons learned on NCSX, in: 2009 23rd IEEE/NPSS Symposium on Fusion Engineering, pp. 1–4.
- [48] Trefethen, L.N., Weideman, J.A.C., 2014. The exponentially convergent trapezoidal rule. *SIAM Review* 56, 385–458. doi:10.1137/130932132.
- [49] Wechsung, F., 2020. `florianwechsung/pyplasmaopt`: Release accompanying the submission of "single-stage gradient-based stellarator coil design: Optimization for near-axis quasi-symmetry". URL: <https://zenodo.org/record/4058482>, doi:10.5281/ZENODO.4058482.
- [50] Wechsung, F., Giuliani, A., Landreman, M., Cerfon, A., Stadler, G., 2021. Single-stage gradient-based stellarator coil design: stochastic optimization. *arXiv:2106.12137*. *Nuclear Fusion* (revised, Aug 2021).
- [51] Weideman, J.A., Reddy, S.C., 2000. A MATLAB differentiation matrix suite. *ACM Transactions on Mathematical Software (TOMS)* 26, 465–519.
- [52] Wobig, H., 1987. Magnetic surfaces and localized perturbations in the Wendelstein VII-A stellarator. *Zeitschrift für Naturforschung A* 42, 1054 – 1066. doi:<https://doi.org/10.1515/zna-1987-1003>.

- [53] Zarnstorff, M.C., Berry, L.A., Brooks, A., Fredrickson, E., Fu, G.Y., Hirshman, S., Hudson, S., Ku, L.P., Lazarus, E., Mikkelsen, D., Monticello, D., Neilson, G.H., Pomphrey, N., Reiman, A., Spong, D., Strickler, D., Boozer, A., Cooper, W.A., Goldston, R., Hatcher, R., Isaev, M., Kessel, C., Lewandowski, J., Lyon, J.F., Merkel, P., Mynick, H., Nelson, B.E., Nuehrenberg, C., Redi, M., Reiersen, W., Rutherford, P., Sanchez, R., Schmidt, J., White, R.B., 2001. Physics of the compact advanced stellarator NCSX. *Plasma Physics and Controlled Fusion* 43, A237–A249. doi:10.1088/0741-3335/43/12a/318.
- [54] Zhu, C., Hudson, S.R., Song, Y., Wan, Y., 2017. New method to design stellarator coils without the winding surface. *Nuclear Fusion* 58, 016008.